TriDurLE

National Center for Transportation
Infrastructure Durability & Life-Extension

Project ID: 2021-WSU-05

Seismic Performance and Fragility of Retrofitted Reinforced Concrete Bridge Columns to Long-Duration Earthquakes

By

Levi Arnold

William Nickelson

Adam Phillips, co-PI

Christopher Motter, co-PI

Department of Civil and Environmental Engineering
Washington State University
Pullman, WA 99164

for

National University Transportation Center TriDurLE
Department of Civil & Environmental Engineering
405 Spokane Street PO Box 642910
Washington State University Pullman, WA 99164-2910

January 2023

Acknowledgments

This report is based on theses by Levi Arnold and William Nickelson in partial fulfillment of the requirements for a M.S. degree from Washington State University. This research was sponsored by the National Center for Transportation Infrastructure Durability & Life-Extension at Washington State University and by the U.S. Department of Transportation. This support is gratefully acknowledged. Simpson Strong Tie (SST) is thanked for providing in-kind donations of fiber reinforced polymer and resin. Nucor is thanked for in-kind donations of Grade 40 reinforcement used in the test columns and bar fatigue tests. Scott Lewis and Joshah Jennings are thanked for assistance with laboratory testing.

Disclaimer

Table of Contents

EXECUTIVE SUMMARY

The Washington Department of Transportation (WSDOT) has identified concrete bridge columns designed and constructed pre-1974 with Grade 40 steel reinforcement to be vulnerable to significant damage from large earthquakes, including a possible Cascadia Subduction Zone (CSZ) earthquake. This has prompted the development of a seismic retrofitting program by WSDOT to increase the seismic performance of these columns to preserve functionality and responsiveness of life-line routes throughout western Washington. However, the retrofitting strategy used of encasing the vulnerable columns with a steel jacket puts additional cyclic fatigue demand on the reinforcement steel. This research focused on generating fracture predictions of Grade 40 reinforcement for CSZ earthquakes to provide WSDOT with location-specific predictions of bar fracture to aid them in prioritization and planning of their retrofitting efforts. Previous literature has studied low-cycle fatigue failure predictions for constant and variable strain amplitude tests which has led to the development of the Koh-Stephens fatigue model. However, this model is very sensitive to the calibration parameters that are specific to the unique steel that was tested. This project conducted additional constant and variable amplitude reversed cyclic tests on Gr. 40 reinforcement bar to validate Koh-Stephens model parameters, Palmgren-Miner's damage rule, and to estimate model variability. Then, a numerical model was created that accounts for variability and uncertainty in the calibration parameters for different heats and bar sizes of steel that could be encountered in the field using Monte-Carlo simulations. The numerical model was analyzed using longitudinal reinforcement strain histories from 60 ground motions, across 4 locations in western WA, for 8 prototype bridge columns at 5 bridge periods. The four locations analyzed represent the four different major site characteristics found in western WA of inland or coastal and basin or no-basin. Results of the fracture prediction model determined that the probability of fracture increased in locations of deep basins. It was also found that the affected period range of high probabilities of fracture was wider for locations with basins. Column design also affected the probability of fracture with columns having low reinforcement ratios and high axial load ratios resulting in greater probability of fracture.

INTRODUCTION

Many bridges in the western United States, including those built during the Interstate Highway Program in the 1950s and 1960s, have seismically vulnerable reinforced concrete (RC) columns. The seismic performance of many of these bridges is essential to post-earthquake mobility, as bridges are relied upon as critical lifelines into urban centers after natural disasters. Some states, including California and Washington, have introduced retrofit programs to enhance the seismic ductility of vulnerable columns. The retrofit involves wrapping the column with either a structural steel or fiber reinforced polymer (FRP) jacket, which enhances the deformation capacity of the column through improved shear strength and concrete confinement. If the retrofit is properly designed, strength degradation in the column under lateral demands from earthquakes will occur due to fatigue fracture of longitudinal reinforcement rather than concrete crushing.

Geologic evidence indicates that the Cascadia Subduction Zone (CSZ) can produce M9 megathrust earthquakes at the interface between the Juan de Fuca and North American plates (Atwater et al. 1995). Such an event has a 10-14% chance of occurring in the next 50 years (Goldfinger et al. 2012). There has been much uncertainty about the characteristics of the ground motions that would result from a large-magnitude CSZ earthquake, because no seismic recordings are available from such an event. To address this knowledge gap, Frankel et al. (2018) simulated approximately 30 M9 CSZ ruptures. Each physics-based scenario (realization) corresponded to a particular set of assumptions for the characteristics of the rupture (e.g., asperities, rupture direction, extent of rupture). The simulated ground motions have longer durations than strike-slip earthquakes, consistent with ground motions from M8+ subduction zone earthquakes in Maule, Chile and Tohoku, Japan. Previous research on the behavior of steel and FRP jacketed columns has focused on demands from strike-slip earthquakes, without specific emphasis on long-duration earthquake demands. Because retrofitted columns are prone to fatigue fracture of longitudinal reinforcement, long-duration earthquakes are expected to increase the likelihood of failure.

Failure of jacketed columns is expected to occur due to fatigue of longitudinal reinforcement, with longer earthquake duration increasing the likelihood of fatigue fracture. Existing models to predict low-cycle fatigue fracture of reinforcement (Mander et al. 1994; Brown and Kunnath, 2004) were calibrated to test data for reinforcement that was subjected to reversed cyclic loading rather than a stress-strain history from an earthquake. Existing models are also highly sensitive to the calibration parameters, which come from the cyclic test data and vary for different bar sizes, grades, heats (production groups), and eras of steel. This project improved these fatigue models by accounting for some of modeling uncertainties and by conducting additional cyclic testing of reinforcement. The updated fatigue fracture models were used in nonlinear time history analyses to develop retrofitted bridge column fragilities for several locations around western WA.

The objective of the research project was to assess the expected performance and probability of failure of jacket retrofitted bridge columns in Cascadia Subduction Zone earthquakes. Nonlinear time history analyses were conducted for a range of bridges and the results were used to calculate failure fragilities. Failure was considered fracture of the outer most longitudinal reinforcement bars. The research was divided into three phases as follows:

1. Experimental Program: Cyclic testing of grade 40 reinforcement was conducted using both reversed cycle tests and variable amplitude strain histories. These tests were used to calibrate additional Koh-Stephens model parameters.
2. Reinforcement Fatigue Model: A reinforcement fatigue fracture model was developed that accounts for the uncertainty of modeling parameters based on previous cyclic test data of Grade 40 reinforcement.
3. Fragilities for Cascadia Subduction Zone Earthquakes: The existing column models were updated to include the improved fatigue fracture model, and the improved column models were used to conduct nonlinear time history analyses of bridges subjected to CSZ demands. The bridges analyzed included a practical range of periods between 0.25 – 3.0 seconds, four locations around western WA, and eight different bridge column details.

The resulting fragilities developed in this research will inform decision-making by state DOT's in Washington, Oregon, and California. The proposed research addresses TriDurLE research thrust #5: Addressing natural hazards and extreme disaster events that threaten the durability and service life of transportation infrastructure. Understanding the fatigue life of retrofitted columns to extreme natural disasters common in the Western US is critical for the durability and rehabilitation of critical transportation infrastructure.

LITERATURE REVIEW

Retrofitting of RC Bridge Columns

Significant damage to reinforced concrete bridge columns was observed following the 1971 San Fernando, CA earthquake (Fung et al, 1971). Subsequent research led to an improved understanding of the design issues, and, in 1983, AASHTO issued new bridge design guidelines with changes aimed at addressing the issue of nonductile bridge columns in new construction. The seismic vulnerabilities of pre-1971 bridge columns were again exposed by the 1989 Loma Prieta, CA (NIST, 1990; EERI, 1990) and 1994 Northridge, CA earthquakes (EERI, 1994; Buckle, 1994). Based on the damage observed in these earthquakes and research on the topic, a need was identified for seismic retrofit of pre-1971 reinforced concrete bridge columns in areas of high seismicity. Many bridges in the U.S. were constructed prior to 1971, including bridges constructed in the 1950s and 1960s as part of the national Interstate Highway Program. These bridges represent important lifelines for cities in the aftermath of a large earthquake.

The deficiencies in pre-1971 reinforced concrete bridge columns are routinely rehabilitated using steel or FRP jacket retrofits. Recommendations on steel jacket design are provided in the FHWA guidelines (2006) and stem from research (Chai et al, 1991; Priestley et al, 1994a,b). While the use of steel jackets provides enhancement to flexural strength, it limits the spread of plasticity, and Chai et al (1991) recommended that a plastic hinge length should be modeled as being equal to the gap length between the jacket and the footing plus bond slip of the longitudinal reinforcement into the footing and into the steel jacket. Much of the research on steel jackets was conducted in the 1990s, at a time when steel jackets were a more cost-efficient option relative to fiber reinforced polymer (FRP). FRP has become less cost inhibitive with time, and the use of FRP jackets offer a distinct advantage over steel jackets by better accommodating the vertical spread of plasticity, which may be achieved by orienting the FRP fibers in the circumferential direction. The improved spread of plasticity leads to a larger plastic hinge length, which increases the deformation capacity for an FRP jacket relative to a steel jacket. Given that steel jacket retrofits have been used by state DOT's for many decades and remain in-service, both types of jackets will be analyzed in the proposed research.

CFRP Column Tests at Washington State University

Six CFRP retrofitted reinforced concrete bridge columns were tested at WSU. Each test specimen consisted of a column, a footing, and a loading head. A test matrix for the six test columns is provided in Table 1, with drawings of the columns provided in Figure 1. The test columns were nominally identical to those tested by McGuiness (2021), except that carbon fiber reinforced polymer (CFRP) jackets were used in place of steel jackets. Test variables in the experimental study included longitudinal reinforcement diameter, longitudinal reinforcement ratio, axial load ratio, and loading protocol.

Table 1: Test Matrix

Column I.D.	Long. Bar Size	# Long. Bars	A_s/A_g	$P/(A_g f_c')$	H/D	Loading Protocol
C(CFRP)-4.0-#7(1.3)-0.05	#7	10	0.0133	0.05	4.0	Cyclic
C(CFRP)-4.0-#5(1.4)-0.05	#5	20	0.0137	0.05	4.0	Cyclic
C(CFRP)-4.0-#7(2.7)-0.05	#7	20	0.0265	0.05	4.0	Cyclic
C(CFRP)-4.0-#7(1.3)-0.05-EQ	#7	10	0.0133	0.05	4.0	EQ
C(CFRP)-4.0-#7(1.3)-0.05-2X	#7	10	0.0133	0.05	4.0	2x Cyclic
C(CFRP)-4.0-#7(1.3)-0.15	#7	10	0.0133	0.15	4.0	Cyclic

The columns were tested as cantilevers, and the column height, H, was the measured distance from the top of footing to the line of action of the applied lateral load. The height of the circular column section was 9” less than H to facilitate inclusion of the loading head. Column diameter, D, was 24”. All test columns had nominally identical 1” clear cover, c_b, Grade 40 longitudinal and transverse reinforcement, and #3 hoops with a lap-splice length, l_b, of 16” and center-to-center vertical spacing, s, of 8” used as transverse reinforcement. No hooks were provided on transverse reinforcement lap splices.

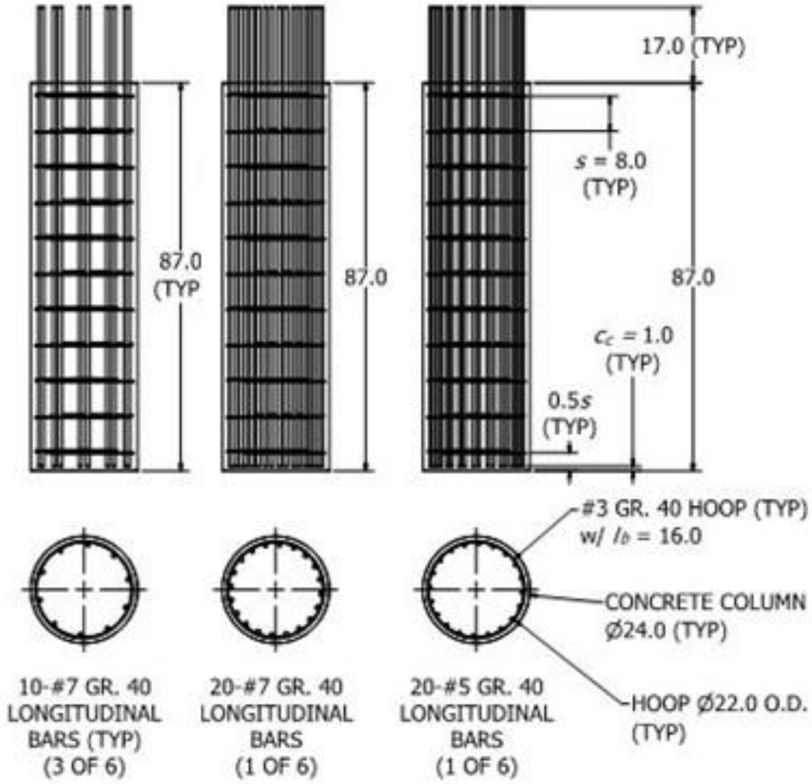

Figure 1: Column Reinforcement Layout

The footing and loading head were consistent with those used in the McGuiness (2021) tests. Voids were provided in the footing using SCH40 PVC pipe to allow the footing to be post-tensioned to the laboratory strong floor and to facilitate lifting and moving of the test specimens before and after testing.

The CFRP jackets were designed to provide a level of confinement stiffness that was greater than that provided by the 3/16” steel jackets used in the columns tested by McGuiness (2021). The specified CFRP modulus of elasticity was 14,200 ksi in the CFRP direction that was oriented circumferentially around the columns. Five sheets of 0.08” thick CFPR were used, resulting in a thickness of 0.40”, which provides circumferential stiffness of 14,200 ksi * 0.40” = 5,680 k/in relative to 29,000 ksi * 0.1875” = 5,437.5 k/in for the steel jacket. The CFRP jackets were used over the lower 24” inches of the column, which is the column diameter. The steel jackets used in the columns tested by McGuiness spanned the full circular portion of the column, except for a 1” gap at the top and bottom.

A fully-reversed cyclic loading protocol was used for four of the six test columns, and one test was conducted using an earthquake loading protocol. These protocols were identical to those used by McGuiness (2021). The reversed-cyclic protocol began with force-controlled cycles, with three cycles each at 5-k, 10-k, and additional intervals of 10-k prior to the yield drift. Displacement control was employed thereafter, with six full cycles each at 1.0, 1.25, 1.5, 1.75, 2.0, and 2.5 times the yield drift, followed by two cycles each at 3.0, 3.5, 4.0, 5.0, 6.0, 8,0, 10.0, 12.5, 15.0, 20.0, and 25.0 times the yield drift, or until the test was completed, shown in Figure 2. For cases in which testing was continued, additional cycles were applied at 25.0 times yield drift, $\delta_y/H.$ C(CFRP)-4.0-#7(1.3)-0.05 used a modification of the reversed cyclic protocol that had twice the number of cycles at each increment. Consistent with the steel jacketed columns tested by McGuiness (2021), the yield drift was taken as 0.4% for C(S)-4.0-#7(1.3)-0.05, C(S)-4.0-#5(1.4)-0.05, and C(S)-4.0-#7(1.3)-0.05-2X and 0.5% for C(S)-4.0-#7(2.7)-0.05 and C(S)-4.0-#7(1.3)-0.15. C(S)-4.0-#7(1.3)-0.05-EQ was tested using an earthquake response history protocol that consisted of a main-shock and aftershock, as shown in Figure 3. For displacement-controlled cycles, the drift used to control the test was corrected to account for footing sliding and rotation.

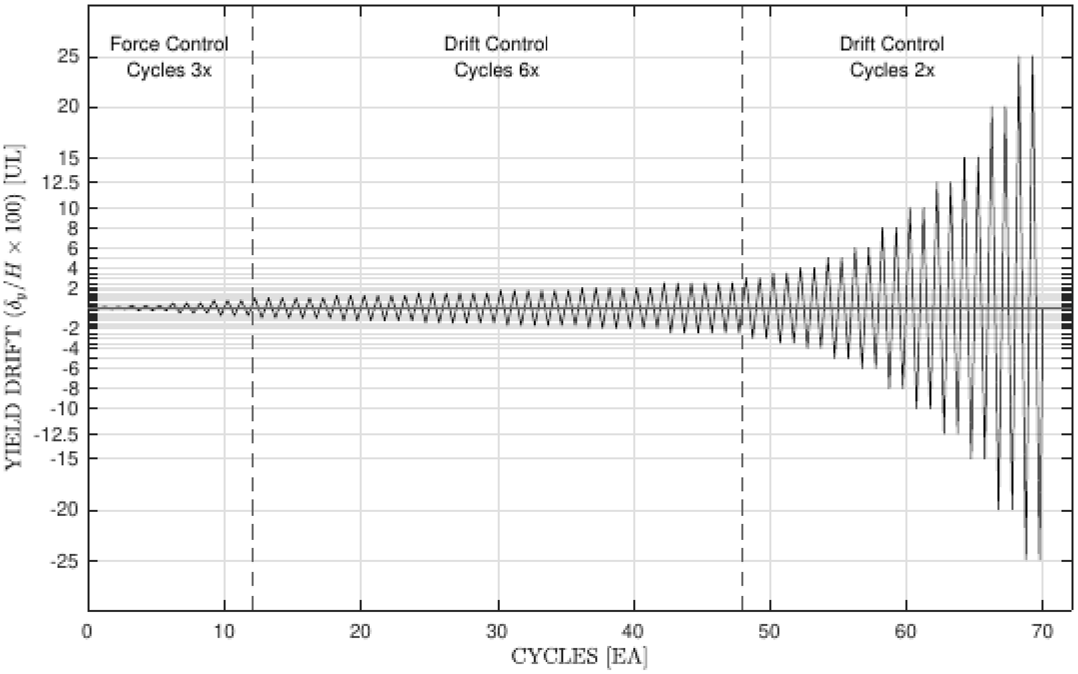

Figure 2: Standard Cyclic Loading Protocol

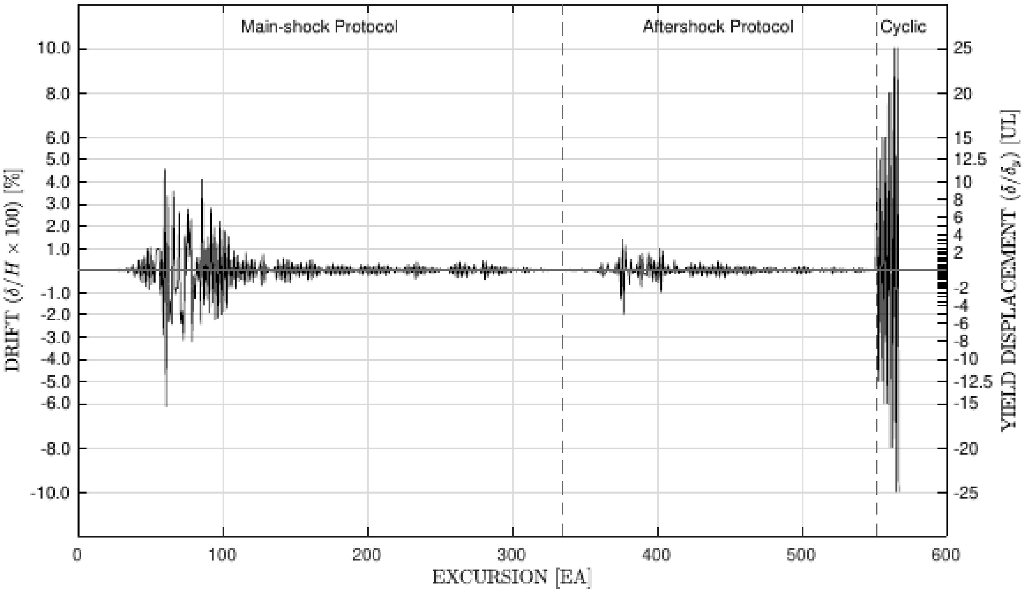

Figure 3: Earthquake Loading Protocol

In all cases, low-cycle fatigue fracture of longitudinal reinforcement occurred near the footing-column interface. The sequence of reinforcement fractures in each loading direction is provided in Nickelson (2022). The lateral load-deformation response is provided in Figure 4 for all tests. All columns were flexure-yielding. In general, minimal pinching is evident in the hysteretic responses, indicative of favorable energy dissipation. The level of pinching for

C(CFRP)-4.0-#7(1.3)-0.15, which incurred damage above the jacketed region, was greater than the other tests. The sequence of longitudinal bar fractures is indicated on the plots, and the degradation in lateral load resistance occurred primarily due to bar fractures.

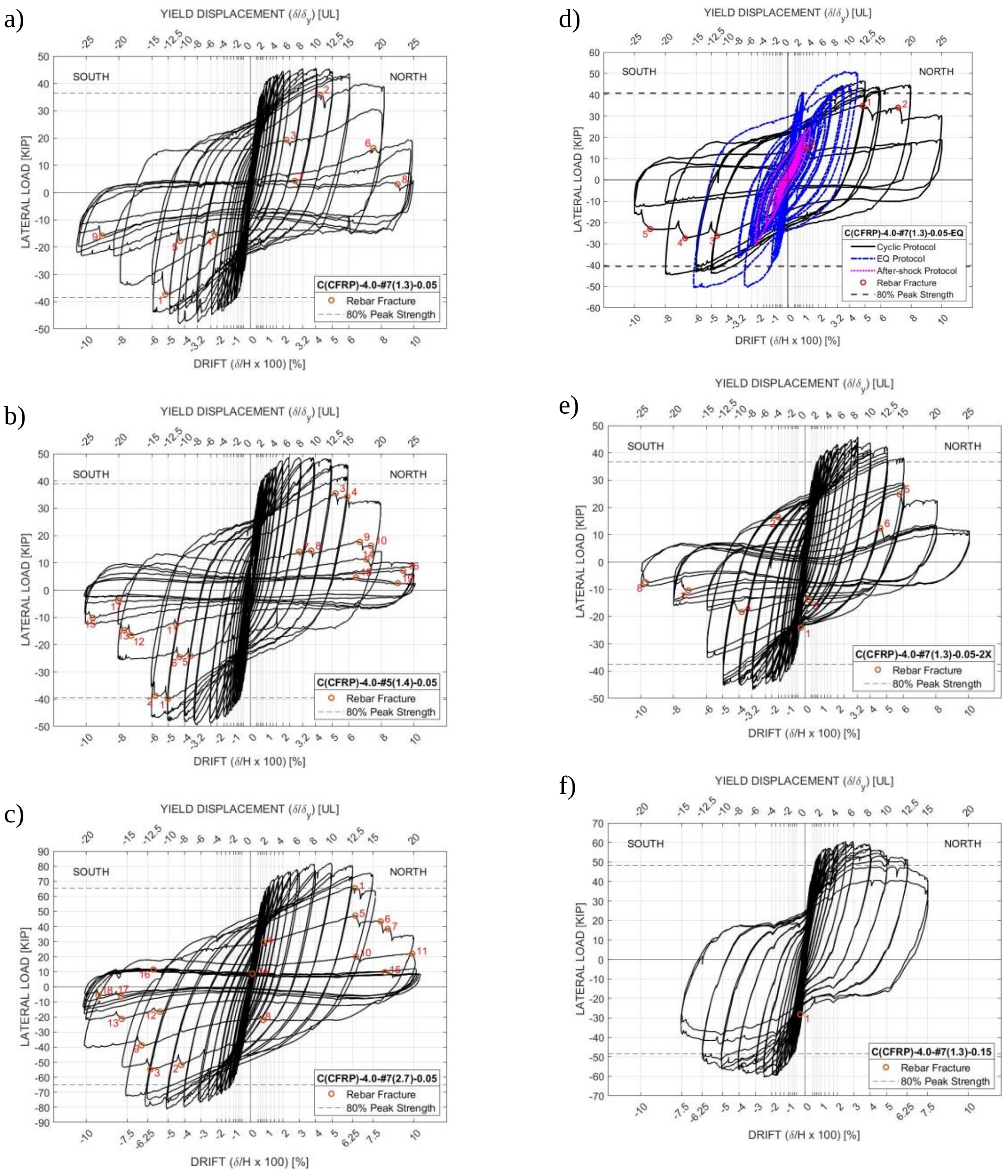

Figure 4: Load-deformation plots of six CFRP column tests (Nickelson, 2022)

Column Numerical Model

The CFRP retrofitted bridge columns were modeled in OpenSEES and validated against the experimental tests. Then, the models were used to conduct nonlinear time history analysis using CSZ earthquake ground motions from across western WA to approximate bridge column fragility. The column model, shown in Figure 5, consisted of a linear elastic line element, a fiber section element over the 1” clear cover to the footing top reinforcement, and a bond slip element at the footing column interface and at 1” into the footing. The spread of plasticity into the column was not modeled, as it was evident from test data that the spread of plasticity in the jacketed region was minimal. The use of a fiber section in the concrete cover was intended to account for the concrete spalling that occurred. This is consistent with the exclusion of cover concrete, which forms a pullout cone, in the Alsiwat and Saatcioglu (1992) bond slip model. The bond slip elements were intended to model strain penetration into the footing and into the jacket. In this model, the plastic hinge length, L_p, was 1”, which was concrete cover dimension, and plastic deformation was modeled to occur in the fiber section element and in the two zero-length bond slip elements. Rotation in the plastic hinge, θ_p, is related to column lateral displacement as:

$$\theta_p = \frac{(\Delta - \Delta_y)}{\left(H + \frac{L_p}{2}\right)} = \frac{\Delta_p}{\left(H + \frac{L_p}{2}\right)} \tag{1}$$

where Δ is the total lateral displacement at the top of the column, Δ_y is the lateral displacement at yield, Δ_p is the plastic lateral displacement, H is the column clear height, and $L_p/2$ is the height of the plastic hinge center of rotation below the base of the column. Previous research (Chai et al., 1991) has shown that plastic curvature in steel jacket retrofitted columns concentrates at the base at the gap between the steel jacket and the foundation. Because L_p is small relative to the height of the column, plastic hinge rotation may be approximated as plastic drift ratio:

$$\theta_p = \frac{\Delta_p}{(H - H_{hinge})} = \frac{\Delta_p}{\left(H - \frac{L_{gap}}{2}\right)} \approx \frac{\Delta_p}{H} \tag{2}$$

This equation results in a linear relationship between plastic rotation and drift ratio. Assuming plane section behavior and uniform strain over the height of the fiber section element, plastic tensile strain in the outermost longitudinal reinforcement, $\varepsilon_{p,t}$, is:

$$\varepsilon_{p,t} = \varepsilon_s - \varepsilon_y = \phi_p(d - c) = \frac{\theta_p}{L_p}(d - c) \approx \frac{\Delta_p/H}{L_p}(d - c) = \frac{\Delta_p/H}{L_{gap} + Cd_b}(d - c) \tag{3}$$

where ε_s is the tensile strain in the outermost tensile longitudinal reinforcement, ε_s is the yield strain of the outermost tensile longitudinal reinforcement, ϕ_p is the plastic curvature, d is the depth to the outermost tensile longitudinal reinforcement, and c is the neutral axis depth. Similarly, the plastic compression strain in the outermost longitudinal reinforcement, $\varepsilon_{p,c}$, is:

$$\varepsilon_{p,c} = \varepsilon_s - \varepsilon_y = \phi_p(c - d') = \frac{\theta_p}{L_p}(c - d') \approx \frac{\Delta_p/H}{L_p}(c - d') = \frac{\Delta_p/H}{L_{gap} + Cd_b}(c - d') \tag{4}$$

where *d'* is the compression strain in the outermost compressive longitudinal reinforcement and Δ_p is from Equation (2) based on the recommendation by Chai et al (1994).

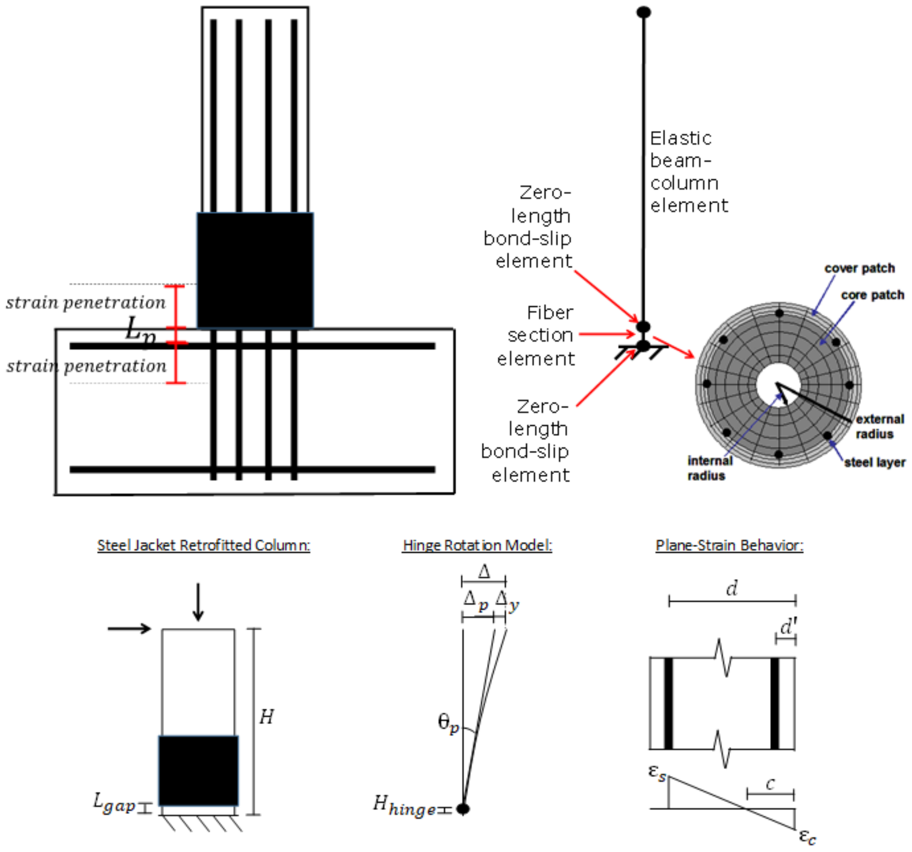

Figure 5: Column Deformation Model

The stiffness of the unjacketed column was determined using the method of Elwood and Eberhard (2009), which accounts for the contribution from flexure, bond slip, and shear as:

$$\Delta = \Delta_{flexure} + \Delta_{slip} + \Delta_{shear} \tag{5}$$

$$\Delta_{flexure} = \frac{H^2\phi_y}{3} \tag{6}$$

$$\Delta_{slip} = \frac{Hd_bf_y\phi_y}{8u} = \frac{Hd_bf_y\phi_y}{8\left(9.6\sqrt{f_c'}\right)} \tag{7}$$

$$\Delta_{shear} = \frac{M_y}{A_vG_{eff}} = \frac{M_y}{(0.85D)(0.2E_c)} \tag{8}$$

where H is the height of the column, ϕ_y is the yield curvature, d_b is the diameter of longitudinal reinforcement, f_y is the yield strength of longitudinal reinforcement, u is the bond stress, M_y is the yield moment, A_v is the area of the cross-section resisting shear, D is the diameter of the column, G_{eff} is the effective shear modulus, and E_c is the modulus of elasticity of concrete. M_y was determined from moment-curvature analysis at first yield of reinforcement. The Zhao and Sritharan (2007) bond slip model was compared to Eq. (7) because of its use in the development of the OpenSees material Bond SP01. Zhao and Sritharan (2007) account for elastic bond slip as:

$$\Delta_{slip} = 0.1\left[\frac{d_b f_y}{4\sqrt{f'c}}(2\alpha+1)\right]^{\frac{1}{\alpha}} + 0.013 \tag{9}$$

where α is the parameter used in local bond-slip relation and was taken as 0.4 as done in Zhao and Sritharan (2007). The increase in stiffness from the FRP jacket was determined by using the approach recommended by Chai et al. (1994) for steel jackets, but without accounting for the bond transfer length needed to reach full composite action. This means that full composite action was assumed over the full length of the jacketed region. The assumption of full composite action is consistent with previous FEM studies on CFRP retrofitted circular bridge columns (Elsanadedy et al., 2012; Mohammed, 2011; Youssf et al., 2014, 2015). As this was an FRP jacket, the gap length, L_{gap}, and grout thickness, t_{grout}, were both zero. The CFRP jacket cured composite tensile modulus and tensile strength were used in place of the steel jacket elastic modulus and yield strength in the Chai et al (1994) method (Nickelson, 2022). Once the stiffness of the column, k, was determined, the elastic flexural rigidity, $(EI)_{elastic}$, of the elastic element, was implemented into the model and computed as:

$$(EI)_{elastic} = \frac{\frac{M_y}{H}\left(H-\frac{L_{gap}}{2}-\frac{L_p}{2}\right)^3}{3\Delta_{elastic}} = \frac{\frac{M_y}{H}\left(H-\frac{L_{gap}}{2}-\frac{L_p}{2}\right)^3}{3\left(\frac{M_y}{Hk}-\phi_y L_p\left(H-\frac{L_{gap}}{2}\right)\right)} \tag{10}$$

where M_y and ϕ_y was determined from moment-curvature analysis using the Mander et al. (1988) confined concrete model. This computation of $(EI)_{elastic}$ accounts for the flexibility in the fiber element based on the displacement at yield due to curvature in the fiber, such that the elastic stiffness in the model is expected to match the computed value for k at yield.

Concrete was modeled using Concrete02 in OpenSees. The Mander et al. (1988) model for confined concrete was used to determine the confined concrete compressive strength, f'_{cc}, and the strain at which f'_{cc} is reached, ε_{cc}. The ultimate concrete stress and strain were modeled as $0.2f'_{cc}$ and $5\varepsilon_{cc}$, respectively. λ in the Concrete02 model, which is the ratio between unloading slope and initial slope, was taken as 0.1. Reinforcement was modeled using ReinforcingSteel. Strain hardening was initiated at 0.01 and strain at peak stress was reached at 0.15. Reinforcement in the bond-slip elements was modeled with Bond SP01. Yield slip, s_y, was computed using Eq. (5-8) from Elwood and Eberhard (2009) utilizing the yield curvature determined from a moment-curvature analysis of the column not accounting for confinement. Slip at ultimate strength, s_u, was taken as 30 times the yield slip, consistent with Zhao and Sritharan (2007). The values for initial hardening slope in the monotonic slip versus bar stress response, b, and the pinching factor for the cyclic slip versus bar response, R_C, were taken as 0.3 and 0.7, respectively.

The stress-strain response of the outermost longitudinal reinforcement at both ends of the column was recorded during the OpenSees analysis. The strain history of the reinforcement was then implemented in the modified low-cycle fatigue model that was used to estimate the point of fracture of the outermost longitudinal bar based on the accumulated plastic strain.

The column model was validated to the six columns tested at WSU and described in the literature review. The fit between model and tests is provided in Figure 6. The model provided a reasonable fit to the test data, except for an overestimate of the level of pinching in the load-deformation hysteresis of C(CFRP)-4.0-#7(1.3)-0.15.

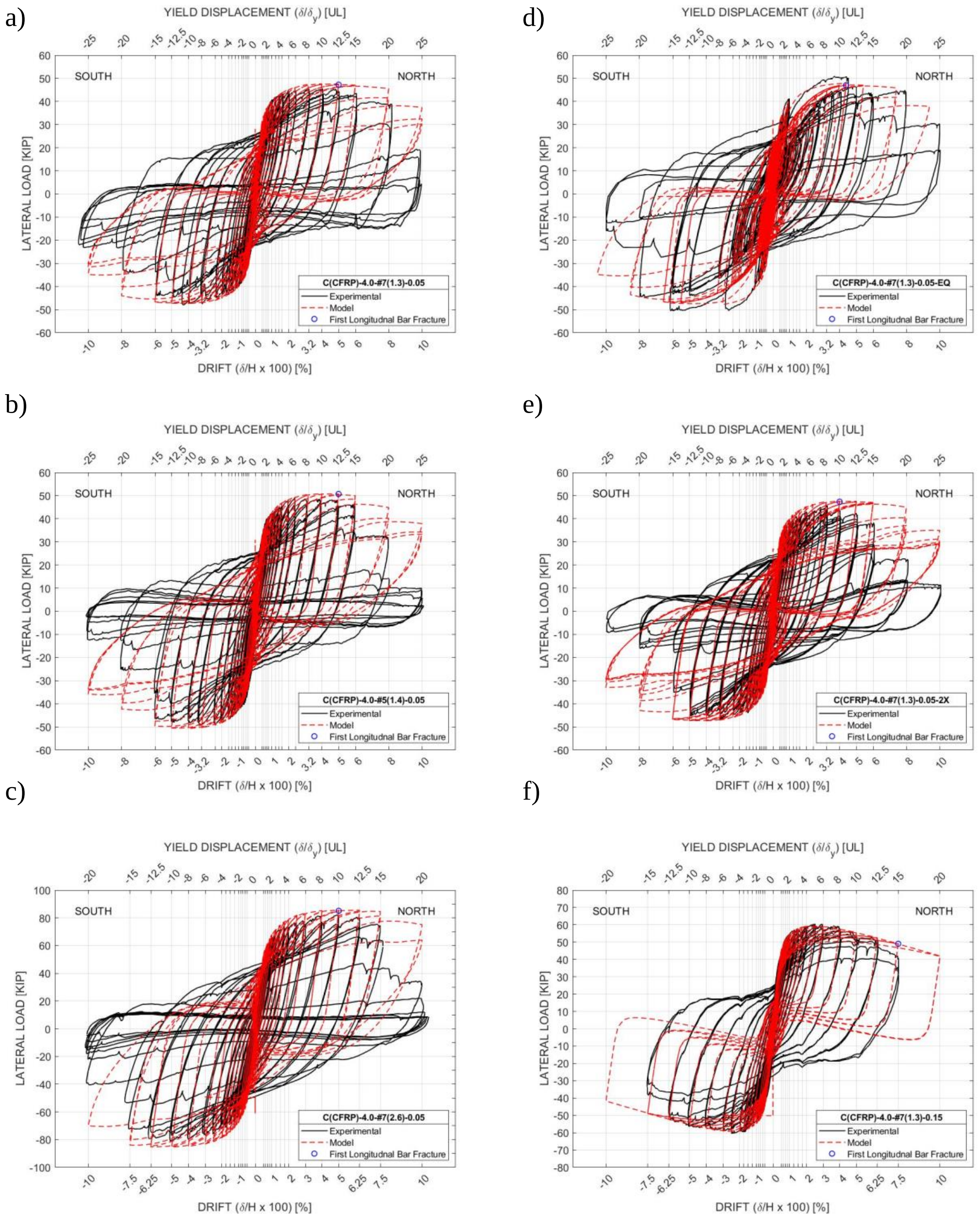

Figure 6: Model fit to experimental tests

Fatigue Fracture Prediction Models

Damage fatigue begins with crack formation usually occurring on the surface of a bar specimen. As cyclic axial strain is applied, the crack grows until the applied force cannot be supported by the remaining bar that is uncracked which causes separation. Mander et al. (1994) reported the difference between smooth and ribbed bars regarding fatigue life. Ribbed surfaces are rolled onto the outer circumferential surface to enhance concrete-to-steel bonding. However, these ribs create stress concentrations at the base of the rib and the nominal bar surface. Due to ribbed bars forming stress concentrations, cracks form earlier in a ribbed bar compared to a smooth bar; therefore, the onset of cracking occurs earlier and fatigue life is diminished (Mander et al. 1994).

Brown and Kunnath (2004) supported this theory of crack formation due to geometric properties of ribbed deformations. The report went further to define the cause of ductile rupture to be the instant where there is no surface area left from the propagating cracks to resist the axial load being applied. Figure 7 illustrates crack formation near the rib face while Figure 8 shows crack propagation as the cycles continue.

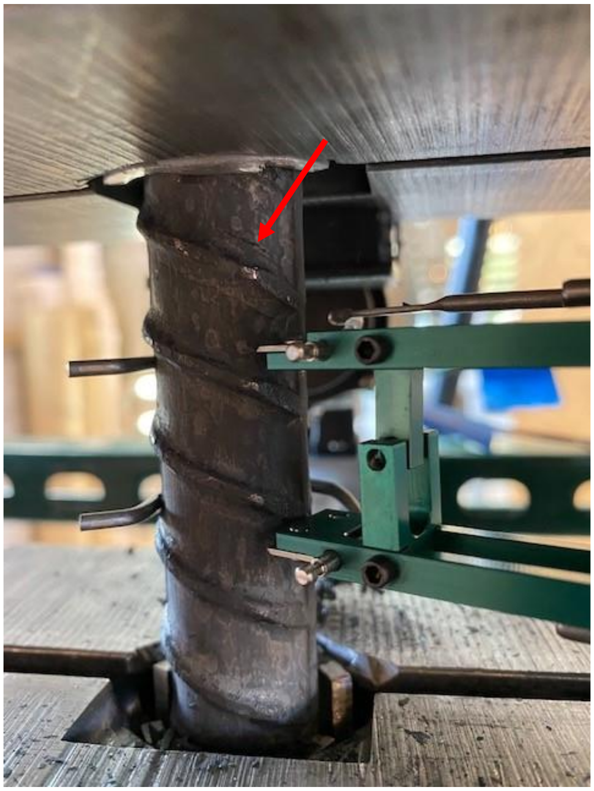

Figure 7: Rebar specimen fatigue crack initiation

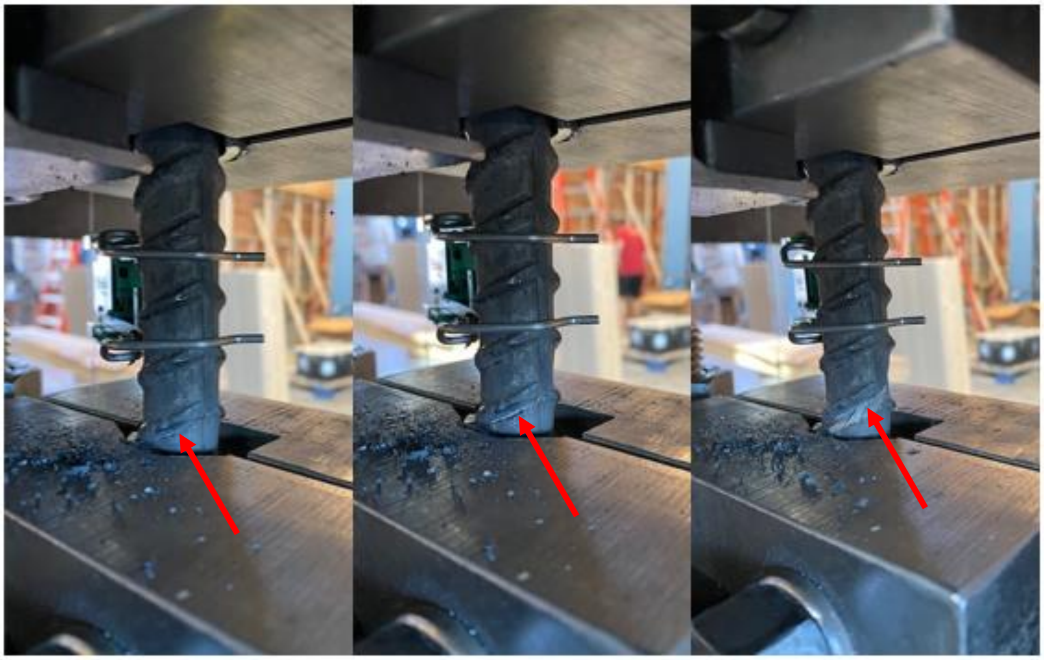

Figure 8: Rebar fatigue crack propagation

Previous studies have developed a relationship between the strain amplitude and number of cycles (tension-compression reversals) until fracture of reinforcement bars for constant strain amplitude protocols. The earlies study conducted by Coffin (1954) and Manson (1953), determined the relationship between plastic strain and cycle content to be a linear log-log relationship between plastic strain amplitude and the number of reversals:

$$\varepsilon_{ap} = \frac{\Delta\varepsilon_p}{2} = \varepsilon'_f (2N_f)^c \tag{11}$$

where, $\varepsilon_{ap} = \frac{\Delta\varepsilon_p}{2}$ is the plastic strain amplitude, ε'_f and c are constant material parameters to calibrate the model, and $2N_f$ is the number of half cycles or load reversals until failure. A study conducted by Koh-Stephens (1991) used this relationship from Coffin-Manson (1954, 1953) to relate total strain amplitude to the number of half-cycles instead of plastic strain. This modification was made because total strain amplitude is an easier measurement to record accurately due to the presence of Bauschinger effects (Barbosa et al., 2017). The modified relationship model by Koh-Stephens (1991) is:

$$\varepsilon_a = \frac{\Delta\varepsilon}{2} = M(2N_f)^n \tag{12}$$

Where $\varepsilon_a = \frac{\Delta\varepsilon}{2}$ is the total strain amplitude, *M* and *N* are the constant material parameters used to calibrate the model, and $2N_f$ is the number of half cycles until failure. Both Hawileh et al. (2009) and Brown and Kunnath (2004) compared several different fatigue fracture models and concluded utilizing the simplified Koh-Stephens model was an accurate method for predicting fatigue life of steel reinforcement. Therefore, the Koh-Stephens (1991) model shown by Equation (2) was used for this study.

The Koh-Stephens model only allows for prediction of fatigue fracture for constant strain amplitude cycles. To predict fracture for variable amplitude strain histories, the Palmgren-Miner damage rule needs to be used to account for cumulative damage. In the application to cyclic fatigue, each cycle of strain contributes to this damage accumulation which is detrimental to the fatigue life. The Palmgren-Miner damage rule, as explained in Dowling (2013), is a ratio of the imparted cycle content to the specimen over the inherent cyclic capacity the specimen is expected to sustain. Each individual cycle ratio is summed to create an index of damage for the loading protocol. When the imparted cyclic content equals the capacity of the specimen, a damage ratio equals 1.0 and fracture is assumed. In application to cyclic fatigue in terms of cycle content, the Palmgren-Miner damage rule is:

$$DI = \sum \frac{2n_f}{2N_f} \tag{13}$$

Where DI is the damage index, $2n_f$ is the number of half cycles at a given strain amplitude imposed by the loading history, and $2N_f$ is the number of half cycle life at the same strain amplitude that a specimen is predicted to have using the Koh-Stephens model.

Steel Reinforcement Buckling

Commonly known in applications to axially loaded columns, as the unsupported length increases, the critical buckling load decreases. This relationship holds true for longitudinal reinforcement, particularly during compression loading cycles. Kashani et al. (2015) tested the effect of inelastic buckling on bar fatigue life with ranging L/D ratios (slenderness ratios) of 5, 8, 10, 12, and 15 while strain amplitude percentages ranged from 1% to 5%. The findings reported relate an increase in slenderness ratio to an earlier onset of cracking and therefore a decreased fatigue life. Aldabagh et al. (2021) also reported on the effect of buckling in low-cycle fatigue in terms of bar diameter which supports the findings of Kashani et al. (2015). It was found that an increase in unsupported length as a function of bar diameter decreases the fatigue life with a 67% reduction from 6d_b to 15d_b (Aldabagh et al., 2021).

A recommendation of an unbraced length of 6d_b or less was suggested by Mander et al. (1994) to avoid inelastic buckling during compression cycles. This recommendation was used by Quesnel (2022) in determining what unbraced length to test Gr. 40 bar specimens. However, many Quesnel's tests using #5 reinforcement bar experienced inelastic buckling at this recommended unbraced length, which was stated to impact the strain reading being recorded by the extensometer (Quesnel, 2022). Due to the same testing equipment and set up being used in this study as Quesnel, bar specimens for this research were tested using 3d_b and 4d_b for unbraced length to try and avoid inelastic buckling.

FATIGUE TESTING

Fatigue Test Setup

Bar tests were conducted in the Washington State University structures laboratory utilizing the testing frame similar to that used by Quesnel (2022) shown in Figure 9. Load was applied to the specimen with a 100-kip capacity actuator controlled with an MTS 407 controller. Data acquisition was completed through a Vishay 5100B scanner.

Figure 9: Testing frame setup

A 100-kip capacity load cell was attached to the cylinder along with a plate attached below for grip connections. Lateral restraint was provided by bolting HSS beams with welded plates to the testing frame. These beams were greased on the inside face for plate-to-beam contact to prevent the horizontal plate from moving out of plane and causing an eccentric load to the specimen. Figure 10 shows the details of the testing frame, equipment, and bracing.

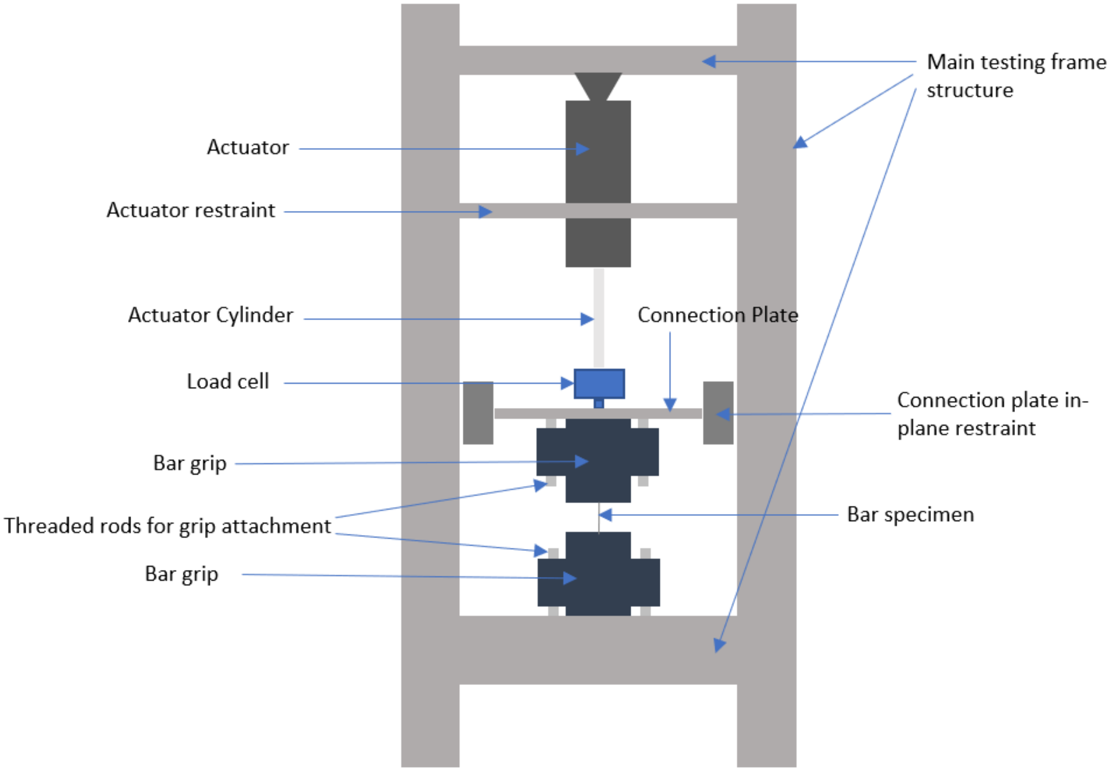

Figure 10: Testing frame diagram with exposed details

Machined steel grips similar to those used by Brown and Kunnath (2004) were used to clamp the top and bottom of the bar specimen. Once clamped around a bar, these grip assemblies were then attached to the lower frame beam and the plate through threaded bolts and nuts. These fixities allowed the grips to transfer the strain from the actuator movement to the unbraced section of the bar specimen. The inside face of the grips allowed space for the specimen to fit between with a ribbed finish. Aluminum tube sections were placed in between the steel grips and the reinforcement bar. This aluminum provided a relatively soft medium between grip and bar to transfer the force from the clamping grip to the bar specimen. Once the two sides of each upper and lower clamp were tightened together, the aluminum deformed around the rebar rib deformations and the grip ribs allowing the grips to engage the rebar during loading. Figures 11 and 12 illustrate the assembly of grip, aluminum, and reinforcement, while Figures 13 and 14 show bar and grip deformations in the aluminum from the grip clamping force.

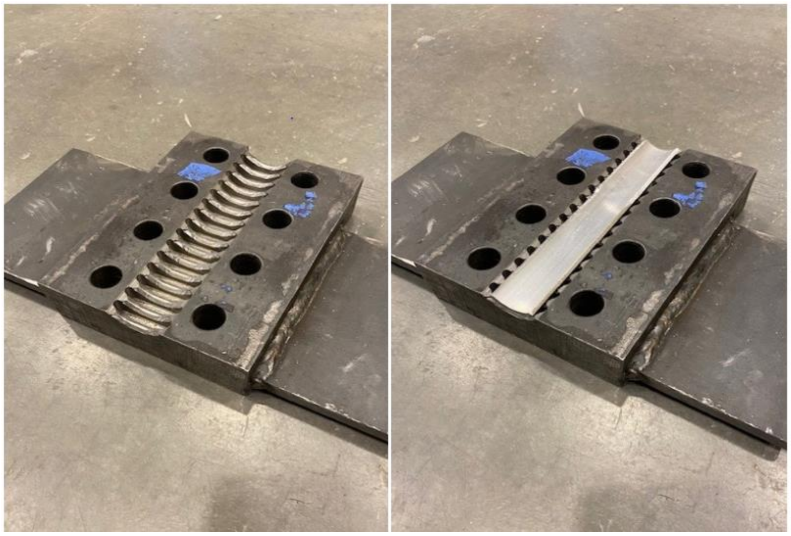

Figure 11: Grip and aluminum assembly

Figure 12: Reinforcement bar placed in aluminum-grip assembly

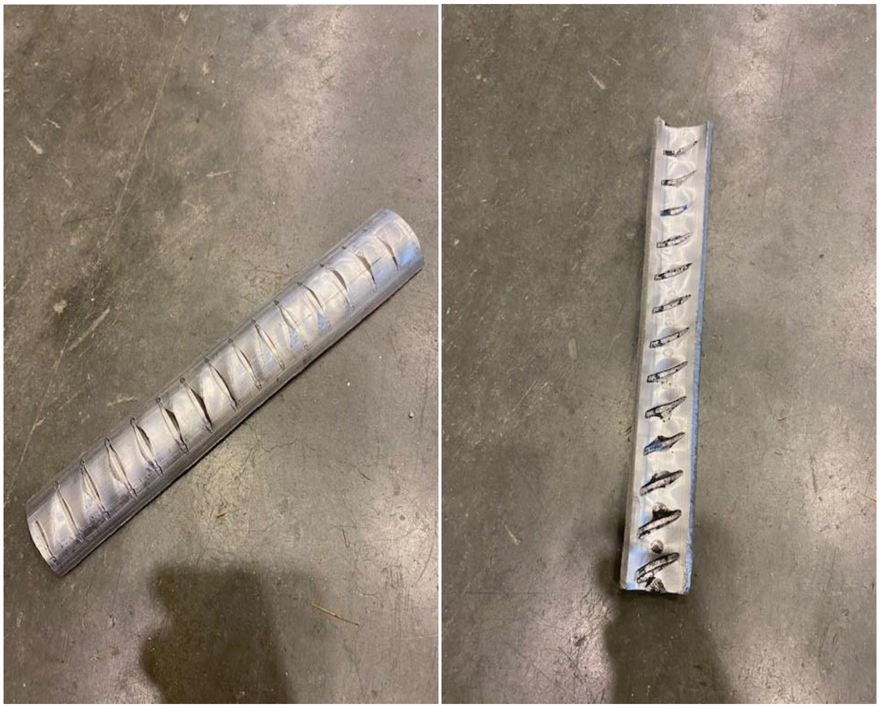

Figure 13: Deformed aluminum removed after testing

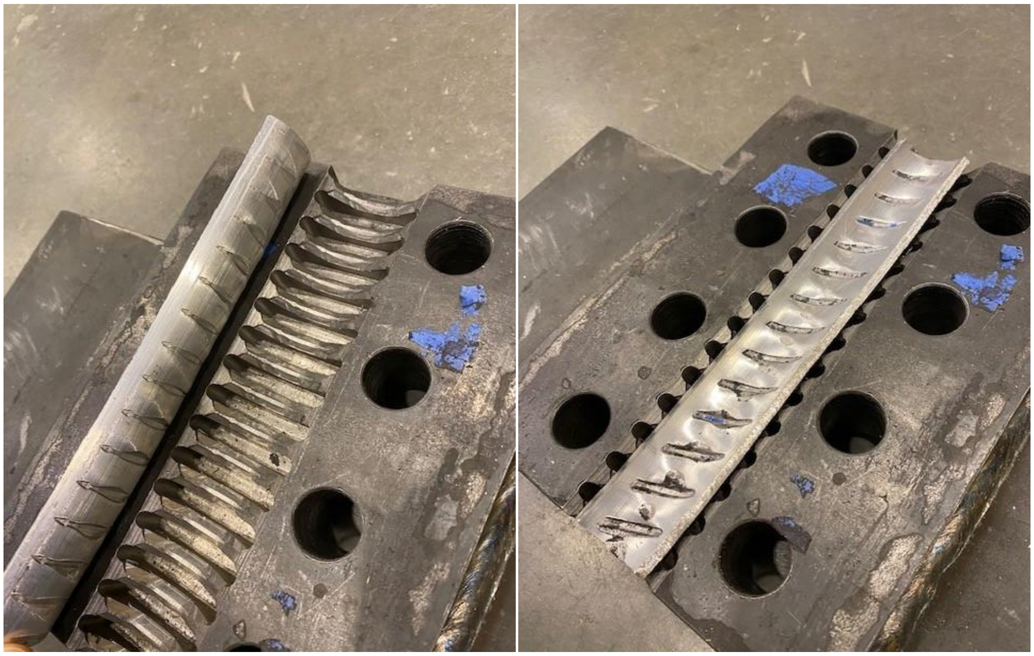

Figure 14: Deformed aluminum from grip ribs and rebar specimen

Several measuring instruments were used throughout various places of the testing setup. A 1-inch extensometer was attached to the unbraced section of bar measured bar strain and served as the control sensor when moving the actuator. The actuator was moved until the desired strain in the bar was reached. A string potentiometer measured the actuator displacement between the actuator body and cylinder. In theory, the actuator displacement readings should match the movement between the two bar grips; however, there were several connections between the actuator and the top bar grip creating a kinetic chain with imperfect axial displacement transfer. Threaded cylinders attached at the end of the actuator cylinder connected coupling adapters, the load cell, and the connection plate. Two string potentiometers were connected from the bottom of the connection plate to the bottom frame beam on each side of the grip and bar assembly. These two string pots allowed recording of actual displacement between the upper face of the top grip and the lower face of the bottom grip which was imparted on the entire bar specimen. It was discovered initial cycles experienced slight bar slip within the grips due to aluminum engagement to the grip ribs and bar ribs. Therefore, these additional grip string pots allowed the bar slip to be quantified in post-processing of test data. Figure 15 below identifies all string pots located within the testing setup used to record displacement data.

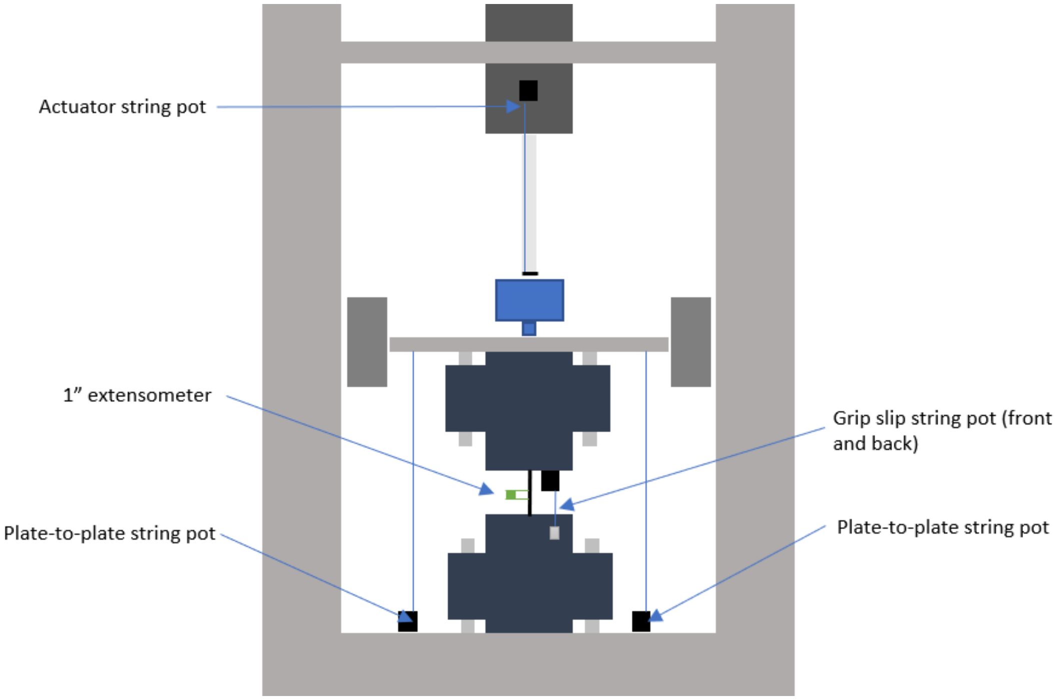

Figure 15. String pot and extensometer sensor placement within test setup

Fatigue Test Methods

Twelve tests were conducted on #5 and #7 bars with most tests using an unbraced length between grips of $3d_b$. This set of tests consisted of five #5 bar tests and seven #7 bar tests with varying loading protocols. The bars used for testing were Grade 40 Nucor bars obtained by Quesnel (2022) and used in the CFRP column specimens tested by Nickelson (2022). Testing began with #5 bars at constant strain amplitude loading protocols with varying mean strain and strain amplitude to generate various points of half-cycles until failures ($2n_f$) in the Koh-Stephens model. Testing shifted to #7 bars beginning with Test 6 running constant and variable strain amplitude loading protocols. Variable amplitude protocols included stepped variable strain amplitudes along with simulated earthquake strain histories, obtained by model data from Bell (2022), which were combined into one loading protocol (Test11). This simulated earthquake loading protocol was sorted from smallest to largest strain amplitude to determine whether the order of strain amplitude cycles impacted the fatigue life of a #7 bar. Refer to Table 2 for the testing matrix stating bar size, unbraced length, strain amplitude, and tension-compression strain values.

Table 2: Fatigue testing matrix

Test No.	Bar Size	Unbraced Length		ε_a	ε_c	ε_t
1	#5	$3d_b$	1.875 in	0.04	-0.02	0.06
2	#5	$3d_b$	1.875 in	0.05	-0.02	0.08
3	#5	$3d_b$	1.875 in	0.04	-0.02	0.06
4	#5	$4d_b$	2.5 in	0.04	0	0.08
5	#5	$3d_b$	1.875 in	0.025	0	0.05
6	#7	$3d_b$	2.625 in	stepped variable amplitude		
7	#7	$3d_b$	2.625 in	0.02	0	0.04
8	#7	$3d_b$	2.625 in	0.0175	0	0.035
9	#7	$3d_b$	2.625 in	0.015	0	0.03
10	#7	$3d_b$	2.625 in	stepped variable amplitude		
11	#7	$3d_b$	2.625 in	earthquake protocol		
12	#7	$3d_b$	2.625 in	sorted earthquake protocol		

During testing of #5 bars, buckling of the specimen's unbraced length was observed during compression cycles. This buckling occurred both in and out of plane of the testing frame. The more buckling the bar experienced the more rotation occurred over the bar unbraced. This rotation of the bar caused interference to the extensometer through contact with the inside face of the grip which interrupted the extensometer reading and compromised control reading used to run the protocol. Figure 16 below demonstrates this interference between grip and extensometer.

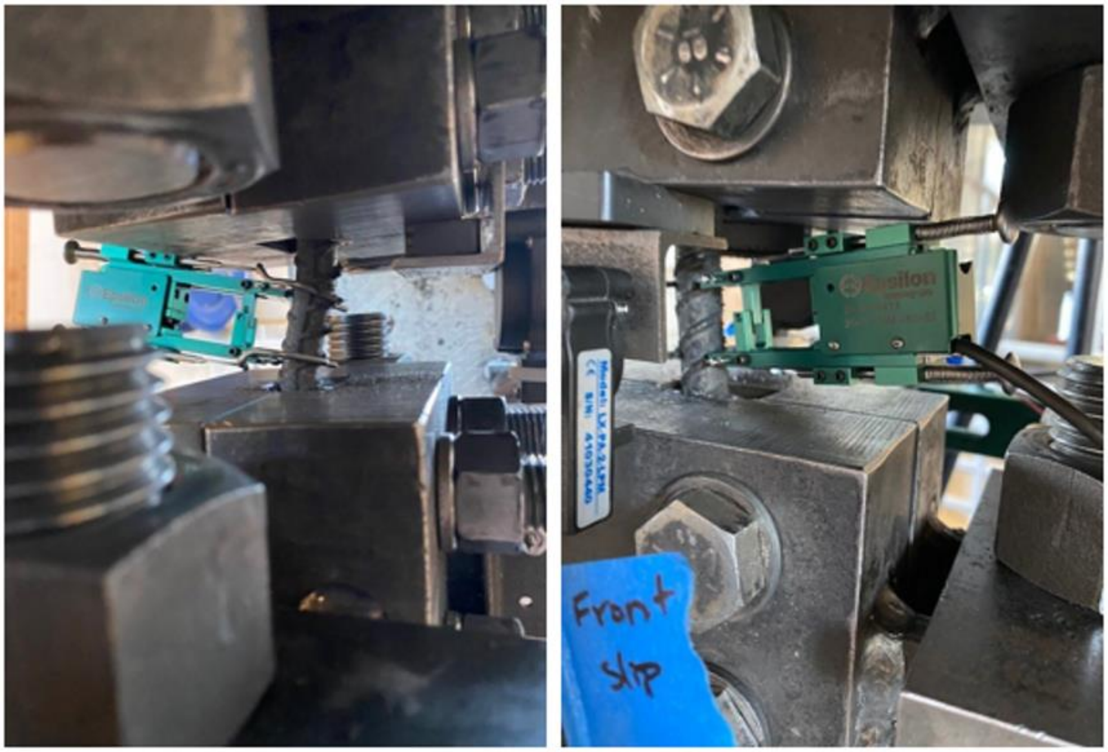

Figure 16: Extensometer-grip contact induced by bar buckling

To address bar buckling, the actuator was straightened and all components connecting the actuator and loading plate were aligned. After still experiencing buckling of the #5 bars, testing shifted to #7 bars which provided an increase in buckling resistance with an increased bar diameter. Once #7 bar tests began, bar buckling was limited, and no contact was made between grip and extensometer therefore preserving the integrity of the extensometer reading.

As a precaution, loading protocols for each #7 bar test began with 10 cycles of 0-1% strain (0.5% strain amplitude). This adjustment allowed the grips to more fully engage the bar specimen through the aluminum at small amplitude cycles which avoided bar slip at larger strain amplitude cycles later in the protocol. Justification for these preliminary cycles came from 0.5% strain amplitude cycles contributing negligible damage to the bar. The cumulative damage imparted on #7 bars from running these preliminary cycles was 0.0085 contributing to an average damage index error of 0.7% across all #7 bar tests with a maximum error of 1.5%.

Constant Amplitude Test Results

Eight constant amplitude tests were completed following the associated loading protocol summarized in Table 2. Failure of a bar was taken to be the complete separation of the specimen where load could no longer be sustained. Figures 17 and 18 below show stress-strain and strain-time histories for Tests 7 & 9 to provide a sample of constant amplitude test results. All test histories can be found in Arnold (2023). Tests 3-5 experienced extensometer difficulties with bar buckling as discussed in the section above. Bar specimens failed prematurely from buckling which caused premature onset of cracking and therefore inaccurate number of cycles at fracture. Table 3 reports the constant amplitude test results of half-cycles at failure, strain amplitude.

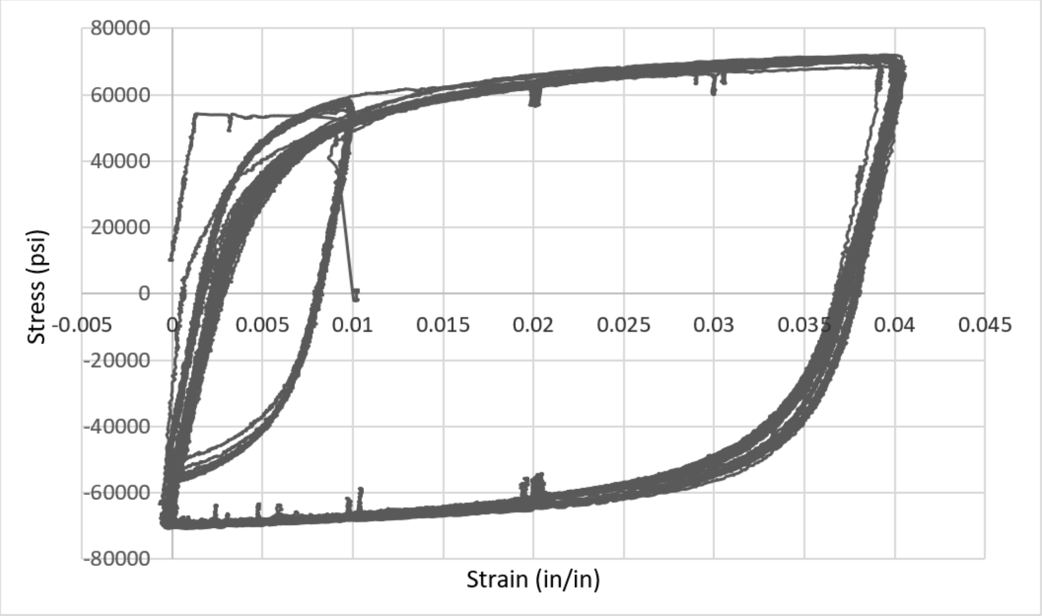

Figure 17: Test 7 stress-strain hysteresis

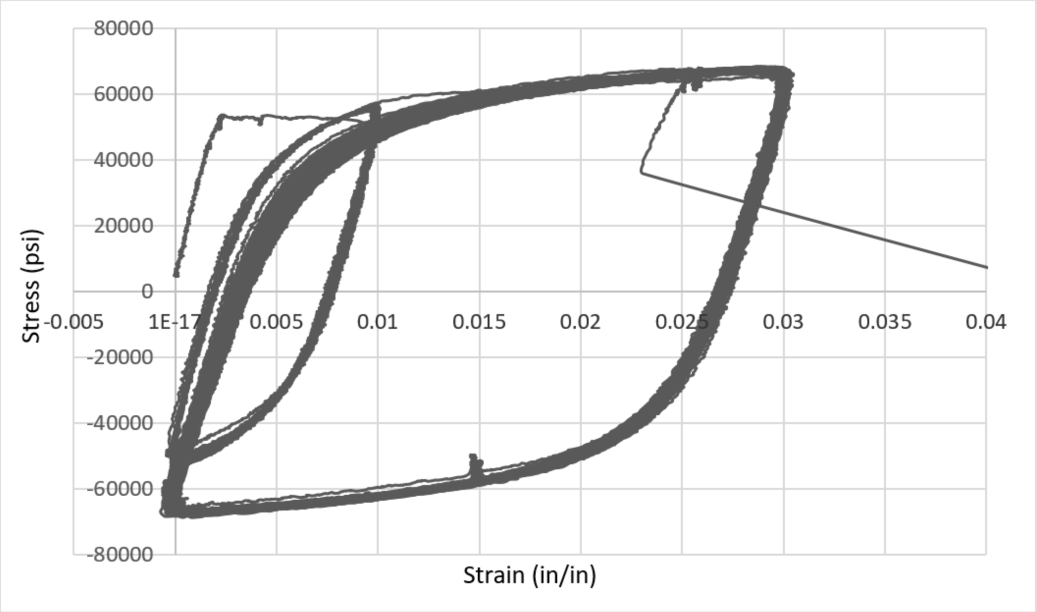

Figure 18: Test 9 stress-strain hysteresis

Table 3: Constant strain amplitude test results

Test No.	**Bar Size**	ε_a	$2n_f$
1	#5	0.04	89
2	#5	0.05	31
3	#5	Data unreliable from instrumentation disruptions	
4	#5		
5	#5		
7	#7	0.02	67
8	#7	0.0175	89
9	#7	0.015	171

Variable Amplitude Tests

Four variable amplitude tests were conducted, two of which incorporated simulated bar strain histories. Three simulated earthquake strain histories were combined to make the protocol for Test 11. These histories all derived from simulated data generated by Bell (2022) for a bridge with a period of 3.0 seconds, ductility ratio of 5.0, and located in Seattle, WA. These strain histories were a relative "worst-case" strain history with numerous large strain amplitude cycles. Protocols for variable amplitude tests can be found in Arnold (2023). Test 11 experienced bar fracture one fifth through the last history while surviving the entirety of the first two ground motions. Lastly, Test 12 protocol sorted the previous protocol by increasing strain amplitude. All cycles within the three histories were combined and categorized from smallest to largest strain amplitude range with failure occurring at the 174th cycle. Test 12 survived all sorted earthquake cycles and underwent constant amplitude cycles between 0% - 3% strain until fracture. Therefore, there is some evidence to suggest that the order of the cycles in a cyclic testing protocol can affect the fatigue fracture life of the bar. Figures 19 - 24 below show all variable amplitude stress-strain and strain-time histories recorded during testing.

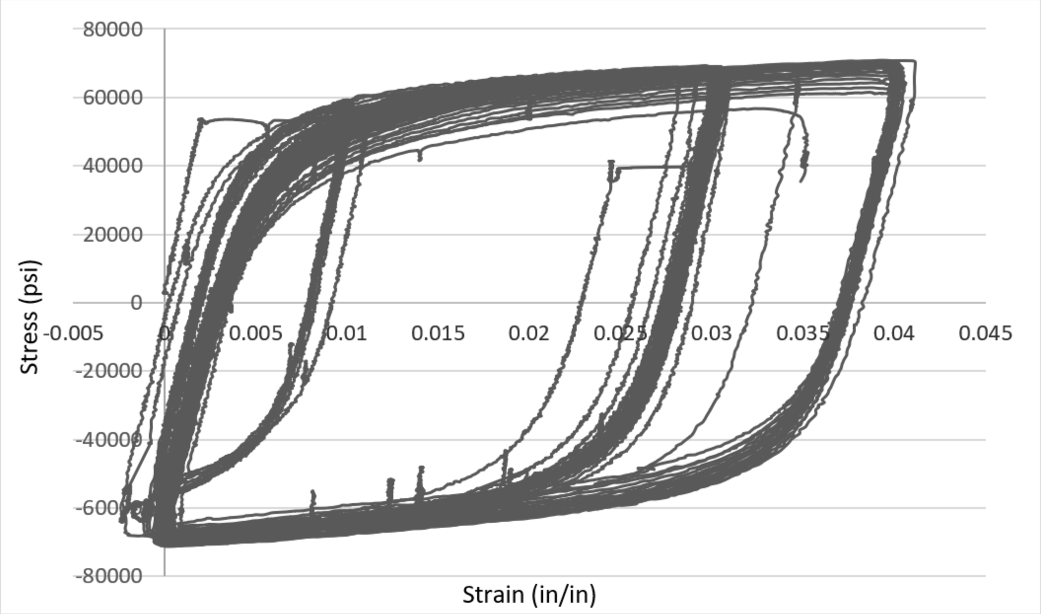

Figure 19: Test 6 stress-strain hysteresis

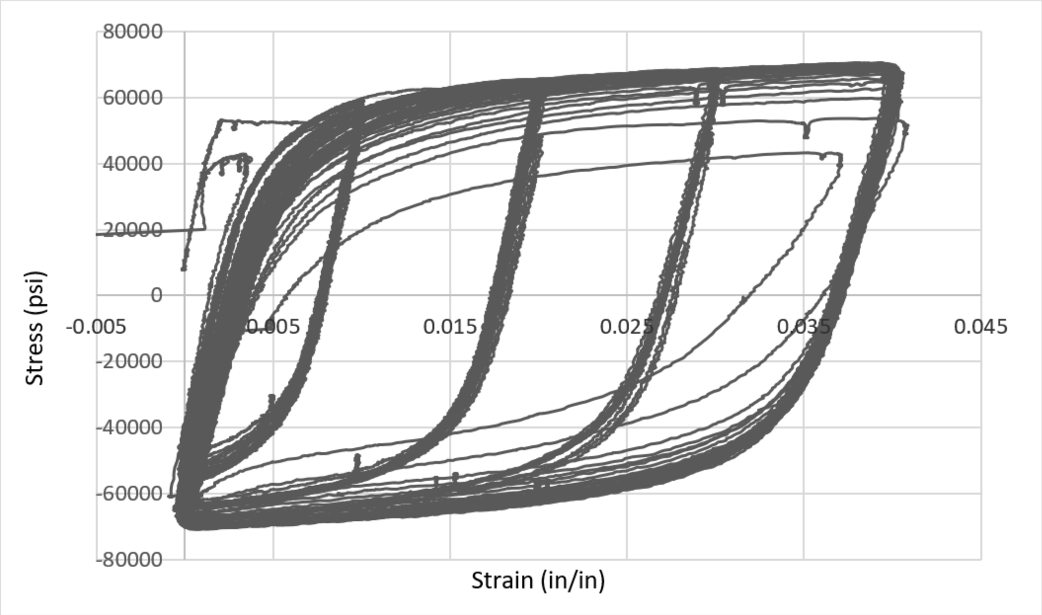

Figure 20: Test 10 stress-strain hysteresis

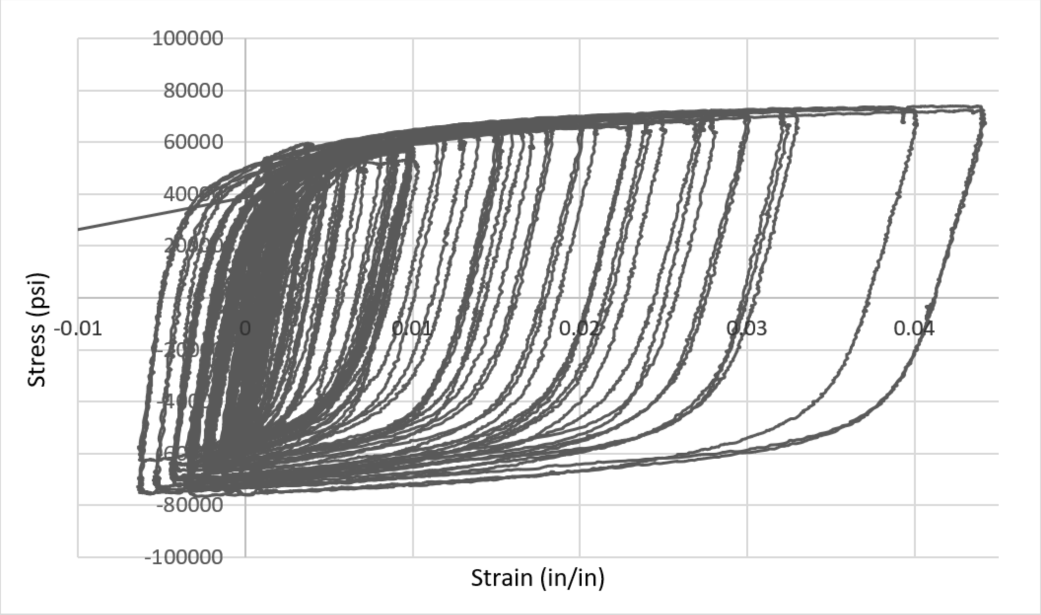

Figure 21: Test 11 stress-strain hysteresis

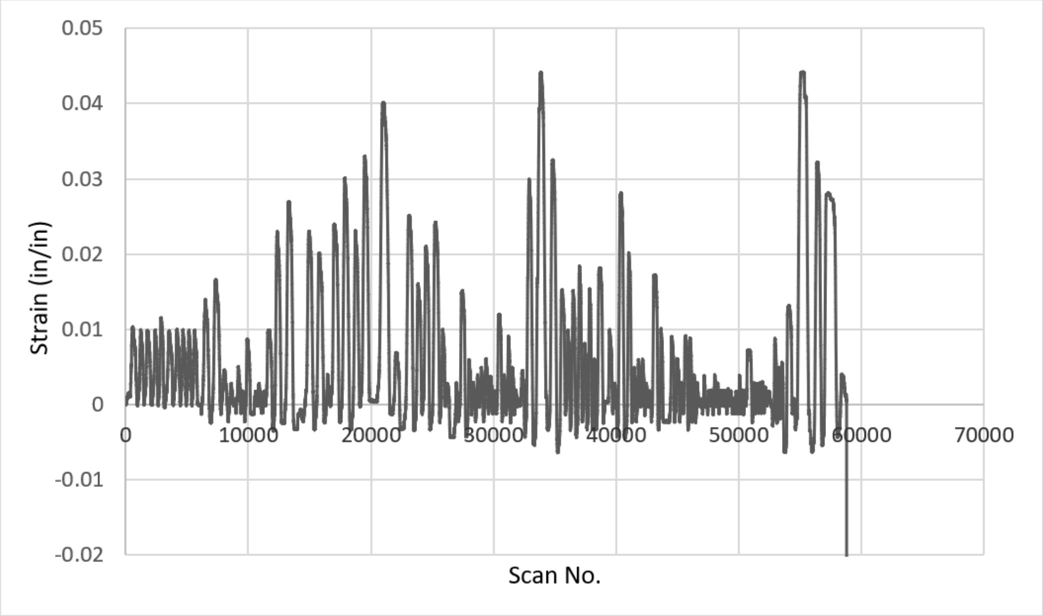

Figure 22: Test 11 earthquake protocol strain history

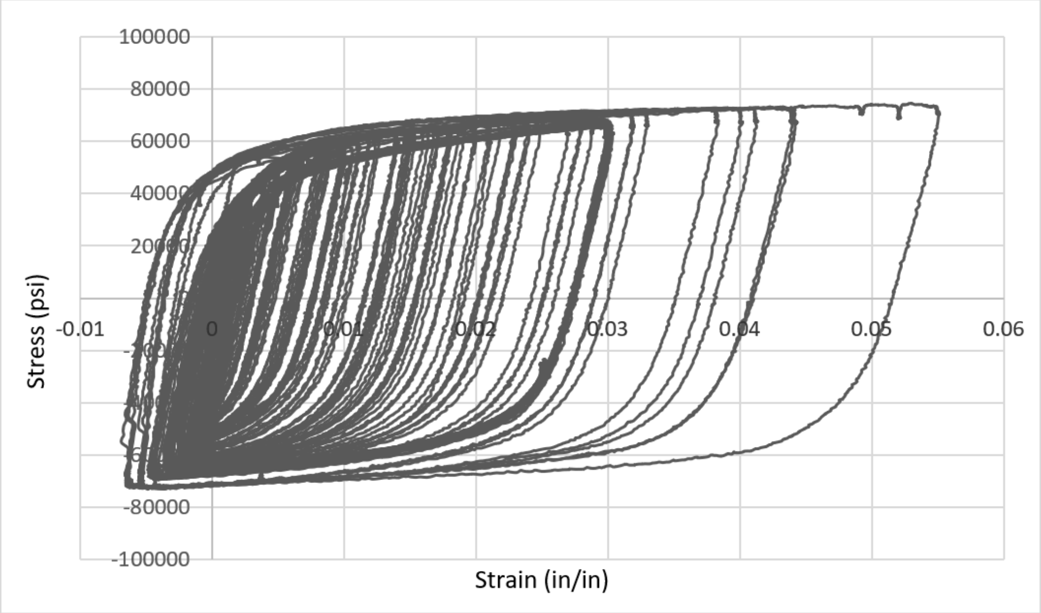

Figure 23: Test 12 stress-strain hysteresis

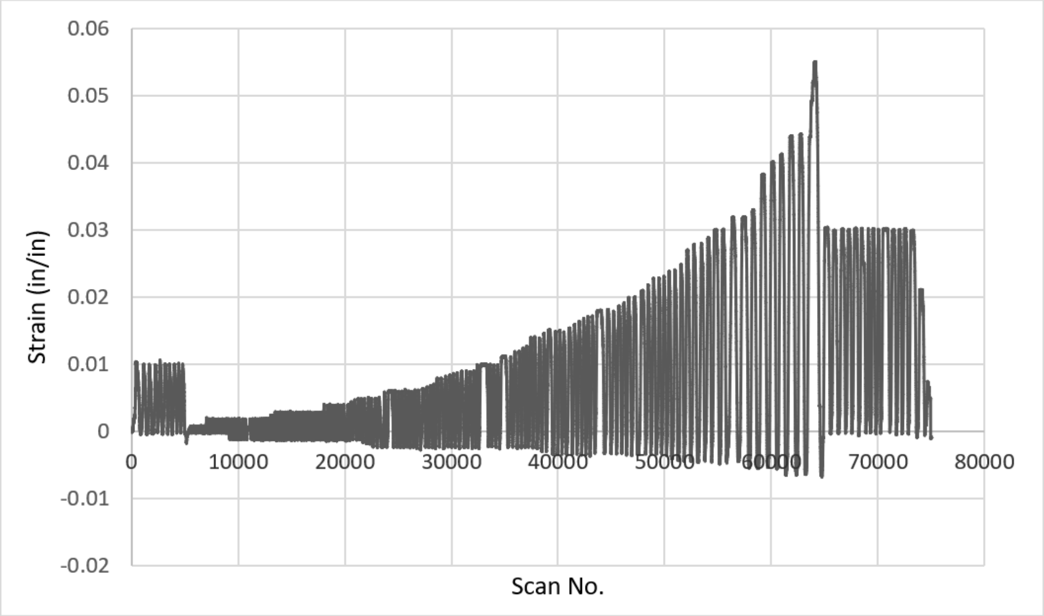

Figure 24: Test 12 sorted earthquake protocol strain history

Fatigue Modeling

Modified Fatigue Numerical Model

Starting with the Koh-Stephens fatigue fracture model presented in Equation (11) the experimental bar test results from this study and other studies were examined. For constant strain amplitude tests, the test data points and Koh-Stephens regressions can be plotted together on a log-log graph, shown in Figure 25. Figure 25 shows several different Koh-Stephens models as well as four sets of experimental bar tests with constant amplitude. All tests were on Grade 40 reinforcement, but vary in bar diameter, era, and material properties (all different heats of steel). The data and regressions presented are from Mander et al. (1994), Brown and Kunnath (2004), Quesnel (2022), and Arnold (2023). Figure 25 shows the variability in material calibration parameters and in fatigue fracture resistance. Figure 25 also shows that the #5 reinforcement bar tests may be unreliable as all 6 data points that are above the Quesnel (2022) upper-bound Koh-Stephens model regression were #5 bar tests from Quesnel (2022) and Arnold (2023). The #7 bar tests were all below the upper-bound model.

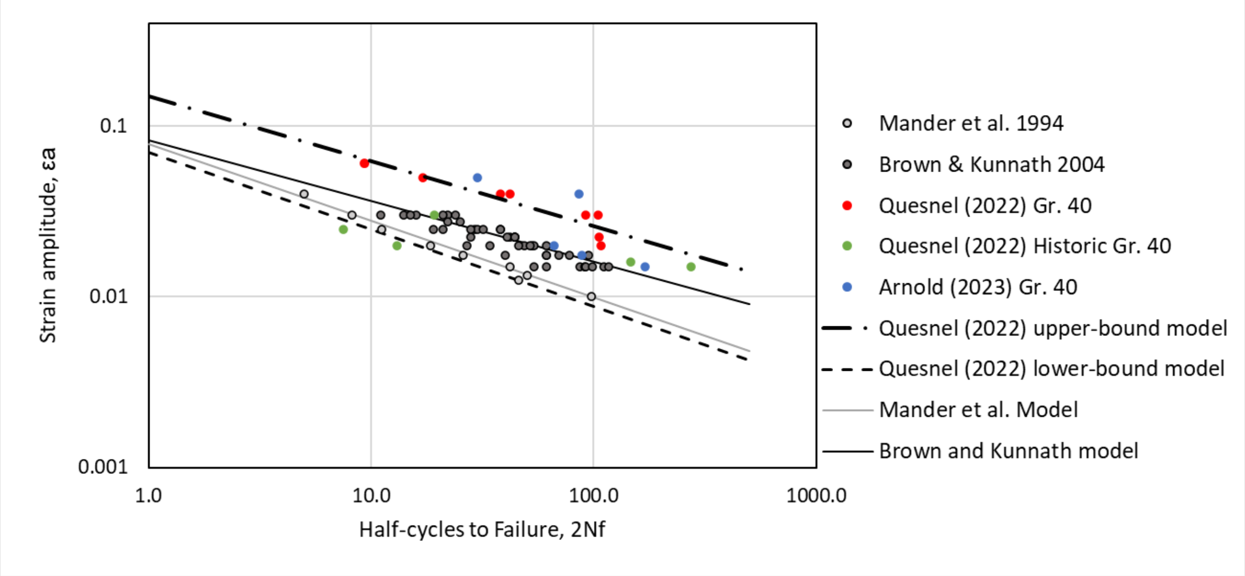

Figure 25: Various Koh-Stephens models compared to different sets of experimental data

To account for the variability in test data and material calibration parameters, a statistics-based approach was employed that used the entire dataset of historic test data from Mander et al. (1994) and Brown and Kunnath (2004) to calculate an average Koh-Stephens model regression. The Quesnel (2022) and Arnold (2023) data was excluded because it differed so substantially from the Mander and Brown data. This could be for a host of reasons including the more modern age of the Grade 40 reinforcement tested or errors in the testing setup. However, since the source of the variability couldn't be identified, the data was excluded from the rest of the analysis. The average Koh-Stephens regression model is shown below and illustrated in Figure 26.

$$\varepsilon_a = 0.0845(2N_f)^{-0.38} \tag{14}$$

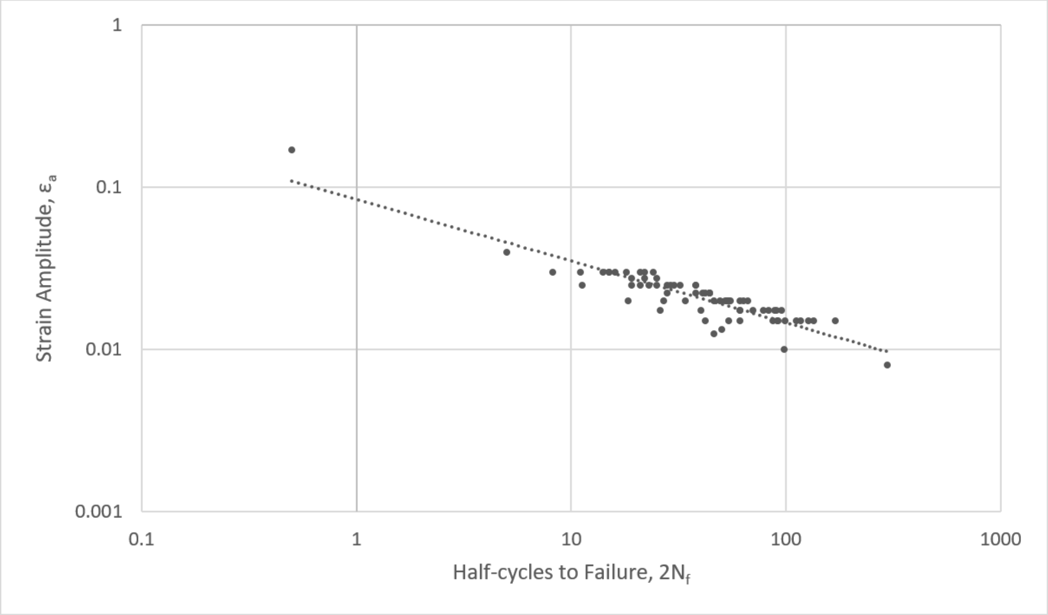

Figure 26: Strain amplitude vs half-cycles, Mander et al. (1994) & Brown and Kunnath (2004)

To account for the variability and scatter in the data, confidence intervals were derived to determine a range of slope and intercept values. To accomplish this, the steps outlined in Xie (2013) were followed to determine the 95% confidence intervals for both slope and intercept. These ranges were calculated to be 0.0720 and 0.0992 for M (intercept) and -0.4228 and -0.3376 for n (slope), respectively. The average and 95% confidence interval regressions are in Figure 27 and shown in Equations (15) and (16). These equations allowed variability in M and n parameters from literature test data to be quantified in later analysis while enveloping the data from Brown and Kunnath (2004) and Mander et al. (1994).

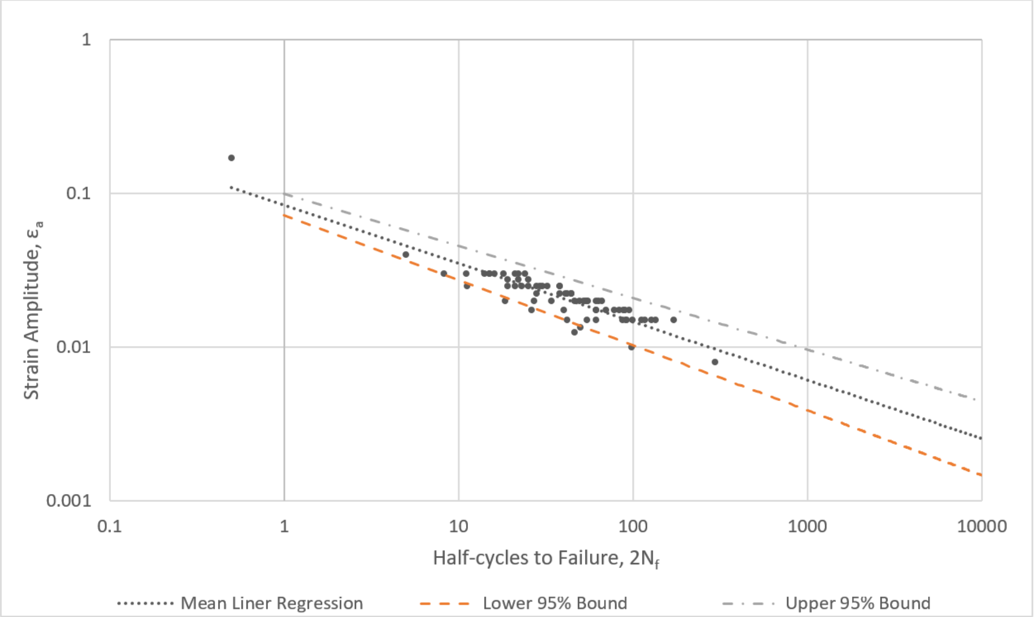

Figure 27: Mean regression and 95% confidence interval bounds

$$\varepsilon_{a,lower\ 95\%} = 0.0720(2N_f)^{-0.423} \tag{15}$$

$$\varepsilon_{a,upper\ 95\%} = 0.0992(2N_f)^{-0.338} \tag{16}$$

Figure 27 was inverted to make strain amplitude the independent variable and $2N_f$ the dependent variable for application to the fracture prediction model. This new plot is illustrated in Figure 28 along with the inverted regressions. These inverted regressions were then used in combination with the OpenSEES column model to predict longitudinal bar failure for a series of bridge columns located across western WA.

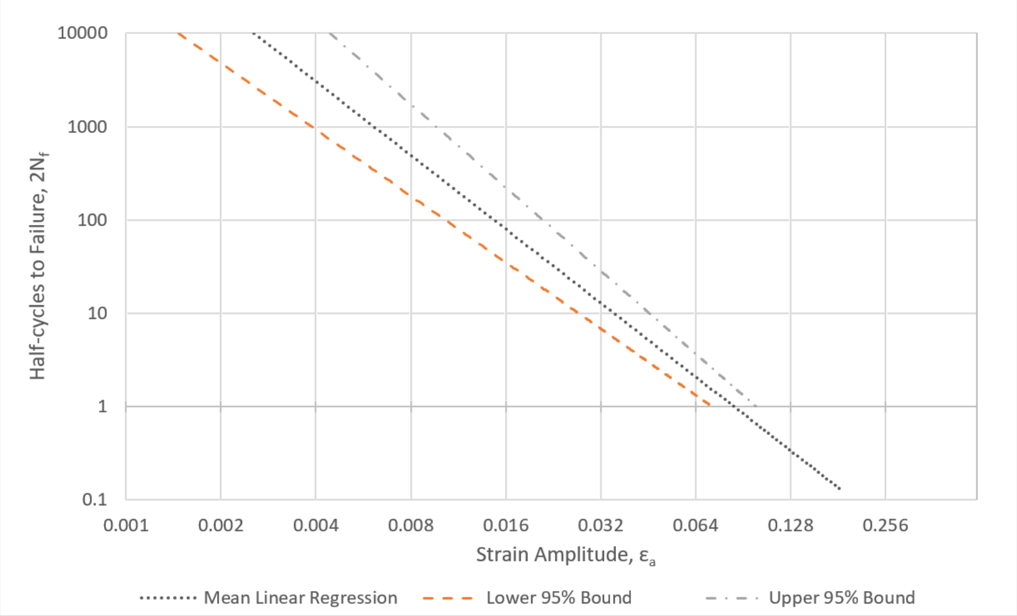

Figure 28. Half-cycles vs strain amplitude regression and 95% confidence interval bounds

$$2N_{f,average} = 0.0015(\varepsilon_a)^{-2.630} \tag{17}$$

$$2N_{f,lower\ 95\%} = 0.0020(\varepsilon_a)^{-2.365} \tag{18}$$

$$2N_{f,upper\ 95\%} = 0.0011(\varepsilon_a)^{-2.962} \tag{19}$$

Column Reinforcement Fracture Fragility Analysis Method

The column model was used to simulate the behavior of retrofitted bridge columns under CSZ ground motions (Nickelson, 2022). The model was analyzed for eight different column designs, bridge periods of 0.25, 0.50, 0.75, 1.0, 1.5, 2.0, 2.5, 3.0 seconds, and ductility ratios of 3.0, 4.0, and 5.0. The simulated ground motions included 30 motions applied in two orthogonal directions, resulting in 60 ground motion histories, for 10 different sites located throughout western Washington. For all these analyses, longitudinal bar strain was recorded for both outermost longitudinal bars in each orthogonal direction providing two bar strain histories per ground motions. This data provided bar strain histories imparted through simulated potential ground motions for use in computing the probability of longitudinal bar fracture for various bridge periods, ductility ratios, and locations. Given the large number of analyses generated by Nickelson (2022), a subset of the data was used to create fracture fragilities for the bridge columns for various locations and bridge types. Strategic data characteristics were chosen to create trends on the probability of fracture data using Monte-Carlo simulations that account for the variability in material calibration parameters for the fracture model.

The eight columns represented varying column design parameters (i.e. longitudinal bar size, number of bars, reinforcement ratio, and axial load ratio). All eight columns were included in the analysis to determine the effect of design parameters on the probability of fracture. Five bridge periods of 0.25, 0.50, 1.0, 2.0, and 3.0 seconds were selected to be analyzed in the fracture prediction model. A constant ductility ratio of 3.0 was chosen across all columns, ground motions, periods, and locations. This variable was kept constant across all selected data to isolate trends of location, column design and period. Bridge inventory in western Washington has reported ductility ratios of 2.0 and 3.5 along lifeline route bridges constructed pre-1974 (Kortum, 2021). Therefore, ductility ratio of 3.0 represented a median bridge column found along a lifeline route in western Washington. The 60 total ground motions represented the x and y components of 30 baseline motions applied in two orthogonal directions (Kortum, 2021). Development of these baseline motions included ground motion recordings at four different sites located in Puget Sound. All 60 ground motions were analyzed on a select bridge column with constant characteristics to determine the ideal probability of failure. Only one of the strain histories (strain1) for each bridge column model was used to calculate the probability of fracture for a given analysis.

Each strain history file coming from the column model was then analyzed using Rainflow counting to obtain the cycle content in the strain history. Dowling (2013) recommends using Rainflow counting to determine the cycle content of an irregular history. This method acknowledged peaks and valleys as points during the loading protocol. The Rainflow function in MATLAB was used, which conforms to the methodology outlined in ASTM E1049 for Rainflow counting (ASTM, 2011). Another method of generating the cyclic content is to record the direct peak-to-valley strain range of each half cycle, without following the Rainflow counting procedure. A case study investigating the effect on damage index using the two methods, Rainflow counting versus direct peak-to-valley counting, was carried out. The findings from this study concluded for a given strain history, the damage index calculated using Rainflow counting was approximately the same compared to the damage index using direct peak-to-valley cycle counting. The maximum percent difference between the two methods was 6.5% with the average error being 3.2%. The results from this case study are summarized below in Table 4 and were generated using column 1, period 3.0 seconds, ductility 5.0, and location 8 from the Nickelson (2022) data. Since Rainflow counting is easily implemented in MATLAB and is the recommended procedure in Dowling (2013), it was used for the fracture prediction model.

Table 4: Cycle counting method case study results

GM ID	**Strain File**	**DI using Rainflow counting**	**DI using peak-to-valley counting**	**% Difference**
4	2	1.039	0.975	6.56
17	1	16.90	16.59	1.86
18	2	1.501	1.462	2.67
27	1	9.531	9.507	0.25
51	1	2.185	4.746	4.75

Figure 29 presents a flowchart of steps used to implement the fracture prediction model that accounts for the variability that is present in the material constants for the fracture model. While this approach does not account for all the possible sources of uncertainty, it does account for some of the large uncertainty seen between the fatigue life of different bars described above.

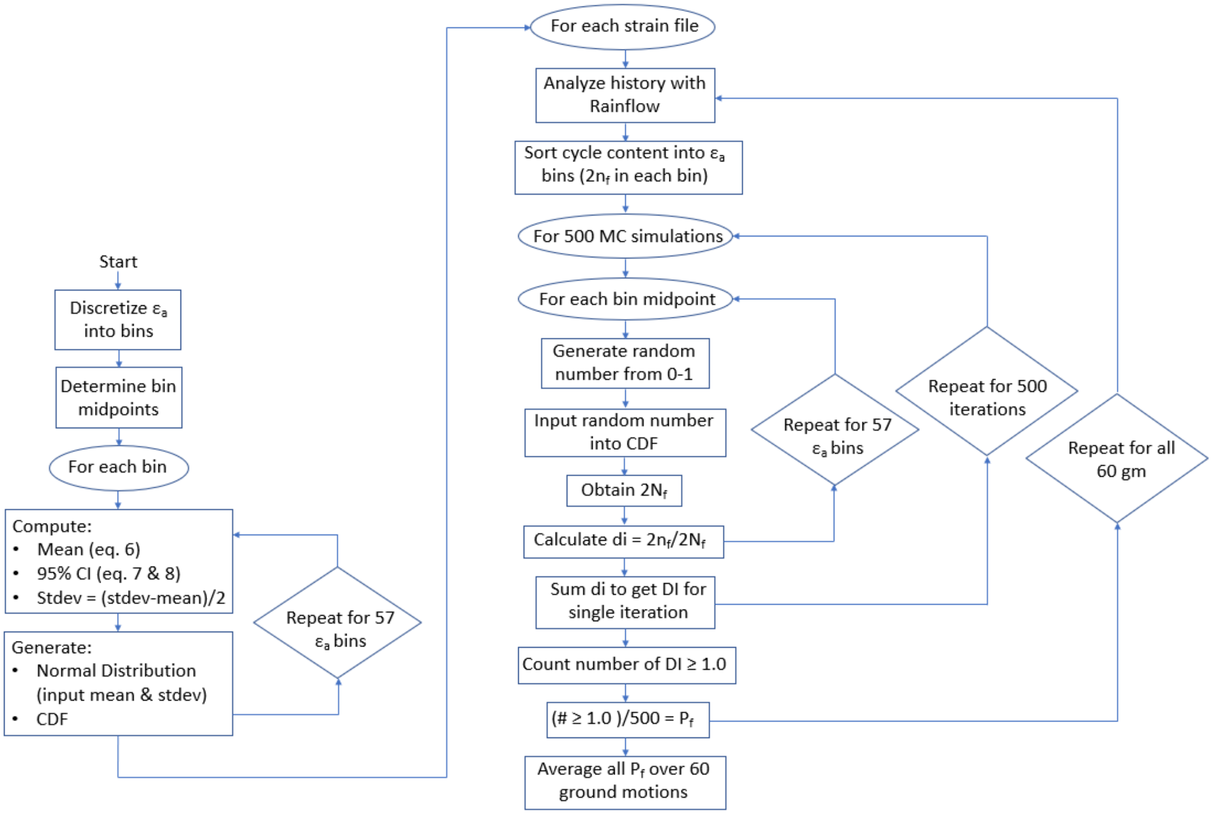

Figure 29: Flowchart of steps in fracture prediction model

With the inverted regressions in Figure 28, various outputs of $2N_f$ can be computed depending on the values of M and n used in the Koh-Stephens model. To enable computation and counting of strain amplitude cycles for many variable amplitude strain histories, the strain amplitude was discretized into 57 bins (refer to Appendix 2 for bin ranges). With these 57 bins, midpoints of each bin were determined for calculations of mean, upper, and lower 95% confidence interval values using Equations (17), (18), and (19). From the 95% values, standard deviation for each bin was calculated. These statistics (mean and standard deviation) were used to generate normal distributions in MATLAB for each strain amplitude bin midpoint. From these normal distributions, cumulative distribution functions (CDFs) of $2N_f$ were generated.

Next, the Rainflow counted ground motion strain histories from the column model analyses were inputted into the model for analysis. Using the previously defined bins, each strain history's cycle content was sorted into these bins for an output table giving the number of half cycles within each strain amplitude bin.

Then, for each strain history, Monte-Carlo simulations determined a synthetic data set of 500 predicted damage values for random Koh-Stephens models falling within the 95% confidence interval. This process was completed for each of the individual Monte-Carlo simulations by first determining a random number between zero and one. This number was inputted into a bin's CDF for an output of $2N_f$ for each bin. A damage index (di) was then computed for each strain amplitude bin (57 total di values) by dividing $2n_f$ from the strain history by $2N_f$ (from the random input to each bin's CDF). All 57 damage indices were then summed to calculate the total damage index (DI) for the motion. This process was repeated through the Monte-Carlo simulation loop 500 times to generate 500 synthetic DI values for a single ground motion strain history. Finally, probability of fracture for that motion was calculated as the ratio of the number of times the DI exceeded 1.0 over the total 500 Monte-Carlo simulations. The Monte-Carlo simulation was completed for every strain history file, providing a probability of fracture for each individual column analysis.

To determine how many Monte-Carlo simulations to use, a small sensitivity study was conducted that determined that 500 simulations was enough to provide accurate results. Using a subset of analysis data from Nickelson (2022), 500 Monte-Carlo iterations resulted in an average probability of fracture of 30%, while 3000 iterations for the same subset resulted in an average probability of fracture of 31%.

The fracture prediction model was analyzed for all 60 ground motion strain histories in the suite of data for a given location, bridge period, ductility ratio, and strain history. Therefore, for one column with a given period and location, there were 60 P_f values and the average P_f could be calculated to be reported. This entire process was repeated for 8 columns, 5 periods, and 4 locations (9,600 strain histories).

Fracture Prediction Model Limitations

The fracture prediction model considered parameter uncertainty within Koh-Stephens M and n parameters, which include experimental uncertainties. These parameter uncertainties include bar-to-bar testing, various bar sizes, different heats of steel, differing test setups from study-to-study, and different researchers. All of the literature tests included virgin steel bars which were never used in a serviced bridge column. While effective in determining fatigue behavior, these uncertainties do not describe those created by being in service. Grade 40 bars in service throughout western Washington have the potential to be subjected to other natural uncertainties in addition to the parameter uncertainties of bar size and steel heats. Previous seismic activity, corrosion, and steel mill imperfections all contribute to a degraded fatigue life within the longitudinal reinforcement of in-service bridge columns which this fracture prediction model does not consider.

Fracture Fragility Results

Fragility Results

As described above, each ground motion's strain1 file iterated through the fracture prediction model resulting in 60 probability of fracture values for one bridge column of one period and one ductility. These 60 values were averaged to present the mean probability of fracture across 30 baseline ground motions applied in two orthogonal N-S & E-W directions of a bridge column (De Zamacona, 2019). The analyzed locations across western Washington were categorized into site characteristics of coastal without basin, inland without basin, inland shallow basin, and inland deep basin. Each site's response spectra were compared to other locations with matching site classification by De Zamacona (2019). The four locations chosen in the fracture prediction model analysis represent a site classification with good geographical spread throughout the state. These locations were Ocean Shores (coastal without basin), Olympia (inland without basin), Port Angeles (inland shallow basin), and Seattle (inland deep basin), shown in Figure 30. Figure 31 maps the final location selections.

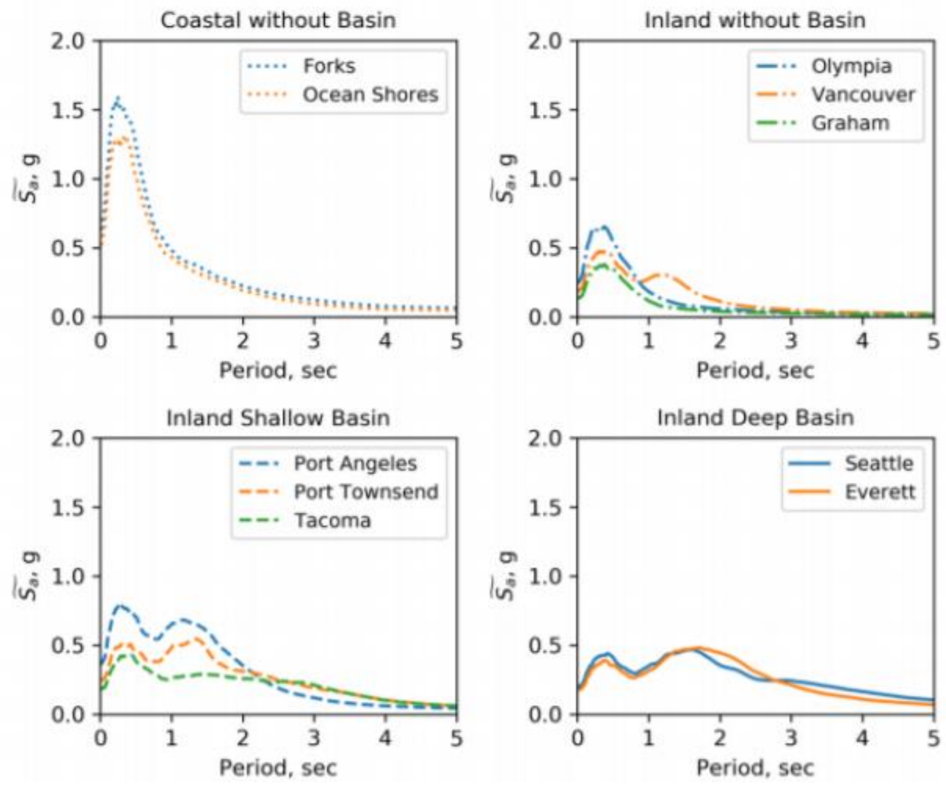

Figure 30: Response spectra of 10 locations (De Zamacona, 2019)

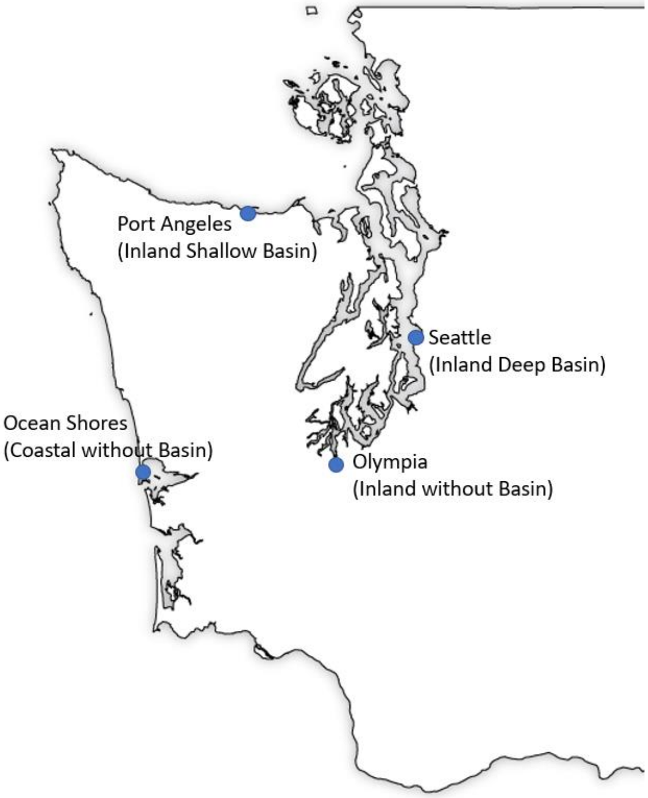

Figure 31: Mapped selected locations in western Washington

Probability of fracture data was analyzed for the effects of period, location, and column design. All average probability of fracture results and standard deviations are presented in Tables 5-8. Figures 32-35 represent plotted results of probability of failure vs period for the four locations.

Table 5: Ocean Shores P_f results

Location 2- Ocean Shores			
	Period	Avg. P_f	Stdev.
col(1) duct(3.0) strain1	0.25	0.242	1.042
	0.5	0.041	0.409
	1	0.090	0.642
	2	0.053	0.456
	3	0.017	0.273
col(2) duct(3.0) strain1	0.25	0.104	0.622
	0.5	0.020	0.263
	1	0.053	0.474
	2	0.019	0.275
	3	0.016	0.269
col(3) duct(3.0) strain1	0.25	0.209	0.946
	0.5	0.009	0.089
	1	0.088	0.641
	2	0.031	0.329
	3	0.017	0.273
col(4) duct(3.0) strain1	0.25	0.112	0.659
	0.5	0.000	0.002
	1	0.056	0.478
	2	0.017	0.273
	3	0.016	0.260
col(5) duct(3.0) strain1	0.25	0.370	1.300
	0.5	0.149	0.796
	1	0.149	0.815
	2	0.112	0.675
	3	0.043	0.416
col(6) duct(3.0) strain1	0.25	0.291	1.146
	0.5	0.085	0.564
	1	0.092	0.643
	2	0.042	0.385
	3	0.011	0.175
col(7) duct(3.0) strain1	0.25	0.273	1.092
	0.5	0.033	0.317
	1	0.075	0.564
	2	0.050	0.433
	3	0.034	0.393
col(8) duct(3.0) strain1	0.25	0.137	0.746
	0.5	0.003	0.035
	1	0.038	0.394
	2	0.018	0.274
	3	0.004	0.260

Table 6: Port Angeles P_f results

Location 3 - Port Angeles			
	Period	Avg. P_f	Stdev.
col(1) duct(3.0) strain1	0.25	0.050	0.491
	0.5	0.117	0.759
	1	0.424	1.403
	2	0.284	1.164
	3	0.082	0.579
col(2) duct(3.0) strain1	0.25	0.045	0.443
	0.5	0.105	0.695
	1	0.332	1.218
	2	0.191	0.904
	3	0.048	0.449
col(3) duct(3.0) strain1	0.25	0.036	0.396
	0.5	0.073	0.578
	1	0.403	1.375
	2	0.273	1.150
	3	0.077	0.559
col(4) duct(3.0) strain1	0.25	0.027	0.327
	0.5	0.066	0.556
	1	0.348	1.248
	2	0.239	1.066
	3	0.030	0.315
col(5) duct(3.0) strain1	0.25	0.070	0.566
	0.5	0.129	0.779
	1	0.484	1.452
	2	0.345	1.267
	3	0.120	0.743
col(6) duct(3.0) strain1	0.25	0.050	0.486
	0.5	0.104	0.704
	1	0.416	1.381
	2	0.271	1.105
	3	0.071	0.527
col(7) duct(3.0) strain1	0.25	0.051	0.485
	0.5	0.090	0.637
	1	0.413	1.386
	2	0.278	1.152
	3	0.087	0.612
col(8) duct(3.0) strain1	0.25	0.027	0.323
	0.5	0.068	0.566
	1	0.319	1.170
	2	0.200	0.940
	3	0.029	0.293

Table 7: Olympia P_f results

Location 4 - Olympia			
	Period	Avg. P_f	Stdev.
col(1) duct(3.0) strain1	0.25	0.0002	0.003
	0.5	0	0
	1	0	0
	2	0	0
	3	0	0
col(2) duct(3.0) strain1	0.25	0	0
	0.5	0	0
	1	0	0
	2	0	0
	3	0	0
col(3) duct(3.0) strain1	0.25	0	0
	0.5	0	0
	1	0	0
	2	0	0
	3	0	0
col(4) duct(3.0) strain1	0.25	0	0
	0.5	0	0
	1	0	0
	2	0	0
	3	0	0
col(5) duct(3.0) strain1	0.25	0.018	0.269
	0.5	0	0
	1	0.005	0.085
	2	0	0
	3	0	0
col(6) duct(3.0) strain1	0.25	0.001	0.011
	0.5	0	0
	1	0	0
	2	0	0
	3	0	0
col(7) duct(3.0) strain1	0.25	0.0004	0.007
	0.5	0	0
	1	0	0
	2	0	0
	3	0	0
col(8) duct(3.0) strain1	0.25	0.0001	0.001
	0.5	0	0
	1	0	0
	2	0	0
	3	0	0

Table 8: Seattle P_f results

Location 8 - Seattle			
	Period	Avg. P_f	Stdev.
col(1) duct(3.0) strain1	0.25	0	0
	0.5	0	0
	1	0.232	1.053
	2	0.643	1.563
	3	0.782	1.550
col(2) duct(3.0) strain1	0.25	0	0
	0.5	0	0
	1	0.175	0.915
	2	0.542	1.471
	3	0.578	1.487
col(3) duct(3.0) strain1	0.25	0	0
	0.5	0	0
	1	0.168	0.912
	2	0.658	1.573
	3	0.692	1.564
col(4) duct(3.0) strain1	0.25	0	0
	0.5	0	0
	1	0.164	0.898
	2	0.545	1.463
	3	0.609	1.549
col(5) duct(3.0) strain1	0.25	0	0
	0.5	0	0
	1	0.308	1.198
	2	0.804	1.541
	3	0.934	1.407
col(6) duct(3.0) strain1	0.25	0	0
	0.5	0	0
	1	0.252	1.081
	2	0.745	1.561
	3	0.857	1.457
col(7) duct(3.0) strain1	0.25	0	0
	0.5	0	0
	1	0.170	0.913
	2	0.650	1.558
	3	0.728	1.530
col(8) duct(3.0) strain1	0.25	0	0
	0.5	0	0
	1	0.157	0.867
	2	0.548	1.467
	3	0.578	1.480

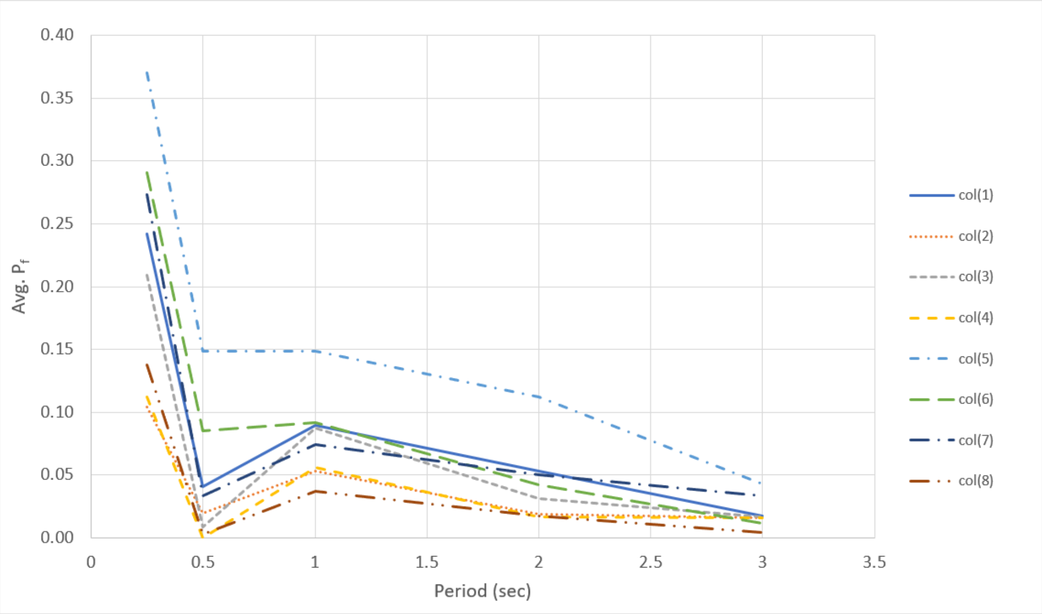

Figure 32: Location 2 – Ocean Shores, WA – Avg. P_f vs Period

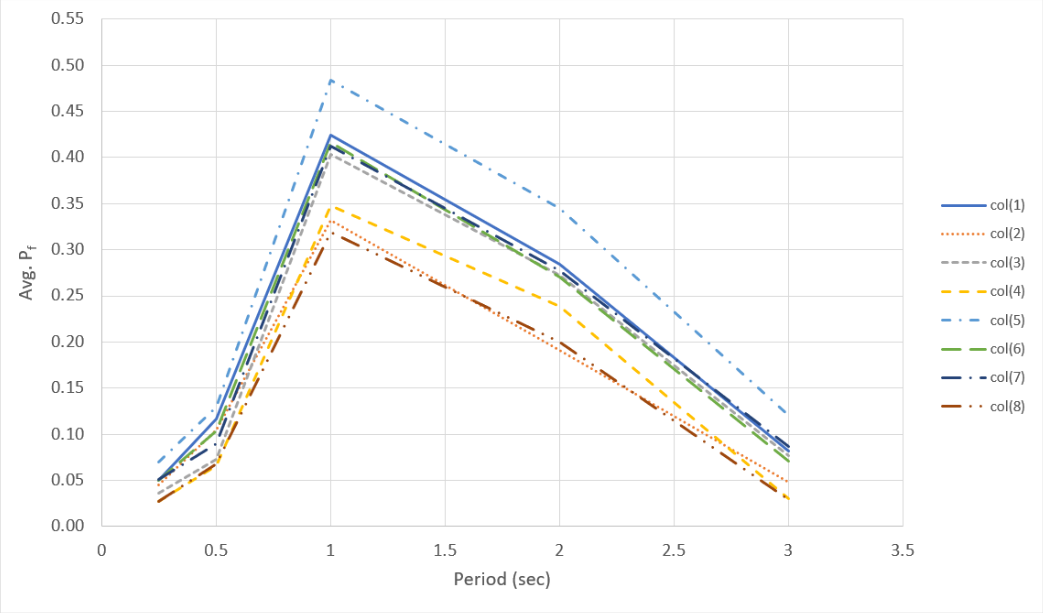

Figure 33: Location 3 – Port Angeles, WA – Avg. P_f vs Period

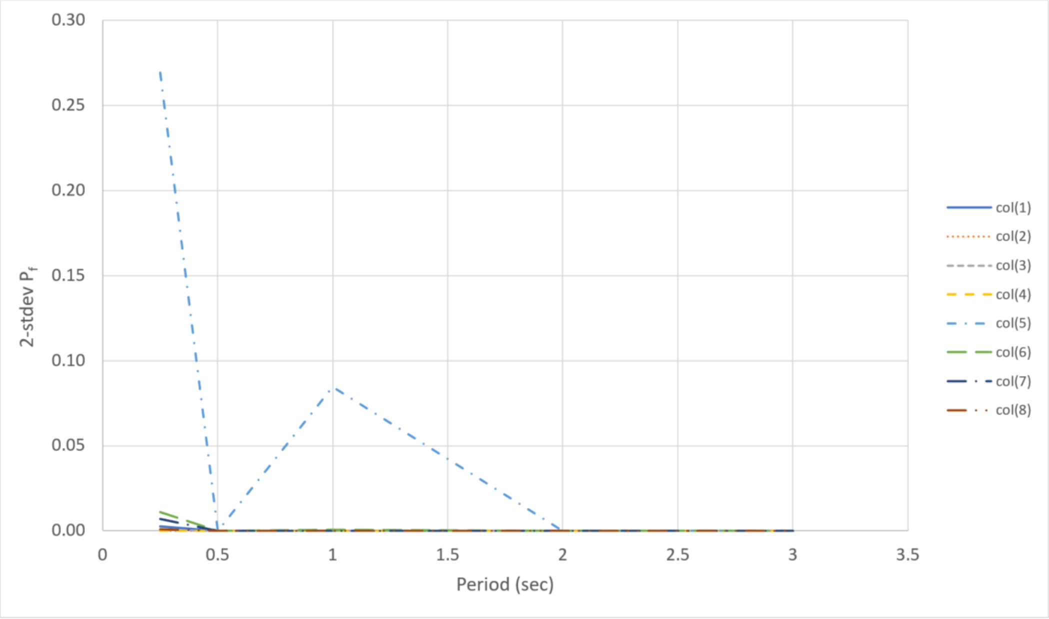

Figure 34: Location 4 – Olympia, WA – Avg. P_f vs Period

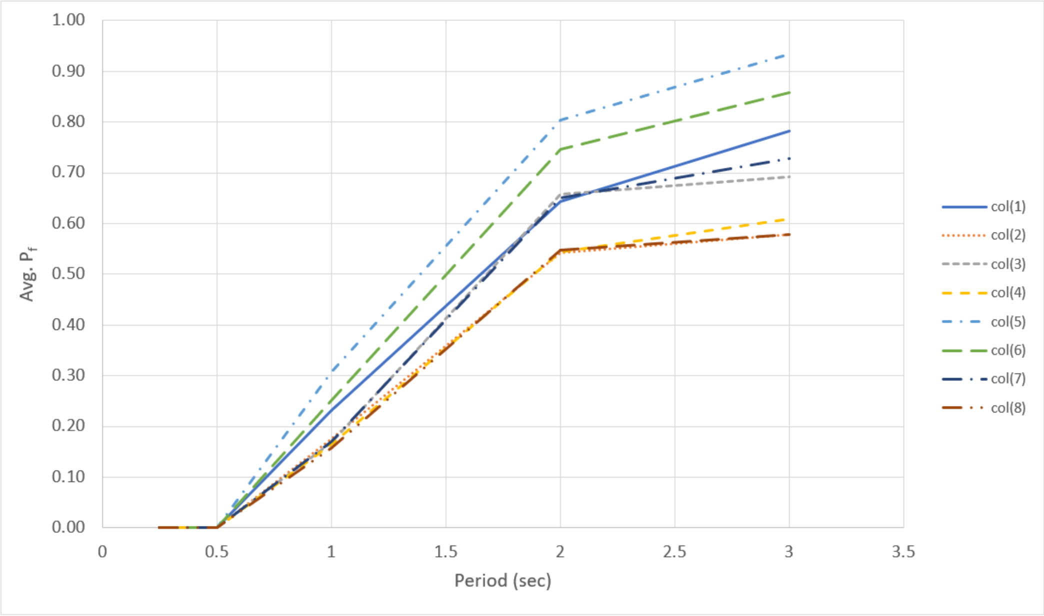

Figure 35: Location 8 – Seattle, WA – Avg. P_f vs Period

Effect of Location and Period

Looking at coastal locations (Ocean Shores), peak P_f occurred at shorter periods with 11% to 37% probability of fracture. Comparing this coastal location to an inland location (Olympia), both without a basin effect, it was determined sites with a “coastal” classification over an “inland” classification was more critical for bar fracture of bridges with periods less than 1.0 seconds. Therefore, coastal locations posed greater concern of bar fracture especially with bridge periods less than 0.5 seconds. For inland locations (Port Angeles, Olympia, Seattle), the severity of basin drives up the period at which peak probability of failure occurs. Additionally, the values of peak probability also increased as basin effects deepened. As seen in Figures 33 and 35, larger values of peak probability of failure were widely spread over bridge periods. This defines the basin effect targeting bridges with larger periods creating greater failure probabilities. Figure 34 indicated inland with no basin (Olympia) was of no concern with peak probability of fracture at 1.8% at 0.25 seconds while all other periods experienced near 0% probability of fracture. For locations with a deeper basin (Seattle), bridges of concern also had a wide spread of periods between 1.0 and 3.0 seconds. Peak P_f results occurred around 2.0 – 3.0 seconds. While 2.0 and 3.0 seconds were the longest periods analyzed, this trend suggested bridges with longer periods of 4.0 or 5.0 seconds could potentially be at greater risk of bar fracture. The overall results were governed by the basin effect with periods of peak P_f increasing as the location’s basin depth increased. A summary table reporting the effect of site classification on probability of fracture and period can be found below in Table 9.

Table 9: P_f results of location, site classification, and period

Location No.	Location Name	Classification	Min. P_f	Max. P_f	Peak P_f Period
2	Ocean Shores	Coastal without basin	0%	37%	0.25 sec
3	Port Angeles	Inland shallow basin	3%	48%	1.0 sec
4	Olympia	Inland without basin	0%	1.8%	0.25 sec
8	Seattle	Inland deep basin	0%	93%	3.0 sec

Effect of Column Design

From the set of plots above, it was also determined column design affected probability of fracture. Column 5 consistently reported the highest probability of fracture values for all locations and periods analyzed. Columns 1, 3, 6, & 7 were consistently grouped together across each location followed by columns 2, 4, & 8. Table 10 below reports each column’s bar size, bar count, reinforcement ratio, and axial load ratio (Nickelson, 2022). Figure 36 illustrates geometric layout of column cross-sections.

Table 10: Column design parameters (Nickelson, 2022)

Col ID	Column Name	Cross-Section Shape	Jacket Type	Long. Bar Size	No. of Long. Bars	Reinf. Ratio (A_s/A_g)	Axial Load Ratio (A_g/f'_c)
1	C(CFRP)-#7(0.9)-0.05	Circular	CFRP	7	16	0.0094	0.05
2	C(CFRP)-#11(0.9)-0.05	Circular	CFRP	11	6	0.0092	0.05
3	C(CFRP)_#7(2.8)-0.05	Circular	CFRP	7	48	0.0283	0.05
4	C(CFRP)-#11(2.8)-0.05	Circular	CFRP	11	18	0.0276	0.05
5	C(CFRP)-#7(0.9)-0.15	Circular	CFRP	7	16	0.0094	0.15
6	C(CFRP)-#11(0.9)-0.15	Circular	CFRP	11	6	0.0092	0.15
7	C(CFRP)-#7(2.8)-0.15	Circular	CFRP	7	48	0.0283	0.15
8	C(CFRP)-#11(2.8)-0.15	Circular	CFRP	11	18	0.0276	0.15

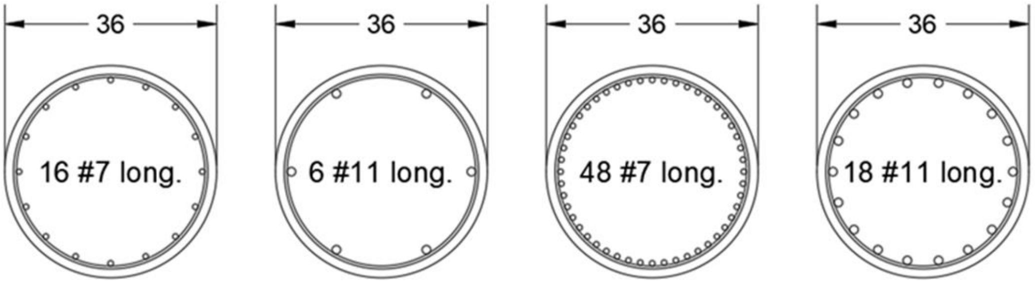

Figure 36: Column cross sections (Nickelson, 2022)

From this provided information, it was concluded columns with low reinforcement and high axial load ratios, represented by columns 1, 3, 5, 6, & 7, yielded governing probability of failure results across all locations and periods. Columns with smaller bar sizes (columns 1, 3, 5, & 7) also experienced greater probability of fracture. Findings by Nickelson (2022) also supported this finding due to increased bond slip of smaller longitudinal bars.

Effect of Ductility

Even though the most common ductility among life-line route bridge columns was 3.0, a ductility case study was performed to determine the effects of increasing design ductility on probability of fracture. Table 11 below demonstrates increased probability of fracture with higher ductility values representing Port Angeles, column 5, period 1.0 second. These supplemental results can be used to adjust prioritization if columns of interest have higher ductility. The higher design ductility means the columns are yielding at a lower force and experiencing greater nonlinear rotation at the plastic hinge. This higher rotation leads to larger bar strains and therefore more accumulated damage, increasing the likelihood that a bar will fracture.

Table 11: Probability of fracture results with changing ductility

Ductility	**P_f**
3.0	0.484
4.0	0.612
5.0	0.714

Results in Context with Historic Bars

Historic Grade 40 bars used in western Washington concrete bridge columns were recovered from demolition by WSDOT. Quesnel (2022) performed constant amplitude tests on these historic bar specimens and the results were plotted and compared to the upper and lower 95% bound regressions in Figure 37. This comparison was made to ensure historic bars within bridge columns in service fell within the 95% confidence interval bound regressions for an accurate application of the fracture prediction model. Reasons for Quesnel's (2022) data showing inconsistencies with literature data statistics include potentially affected historic specimens. Since these specimens were recovered from used bridge columns, there are several reasons for historic specimens to be negatively impacted, the first being previous earthquake activity. If bridges containing these historic bars experienced any seismic ground motion activity, an unknown amount of applied strain prior to lab testing would degrade the fatigue life. Secondly, while Quesnel (2022) cut out straight portions of deformed historic specimens for testing, these testing specimens may have been slightly bent which would have caused inaccurate fatigue behavior. Lastly, corrosion could possibly have affected these bars while in service also degrading the fatigue life. These natural types of uncertainties were unable to be controlled or measured by experimental means and may explain disagreements with Quesnel's (2022) historic data and the 95% confidence interval regressions in Figure 36.

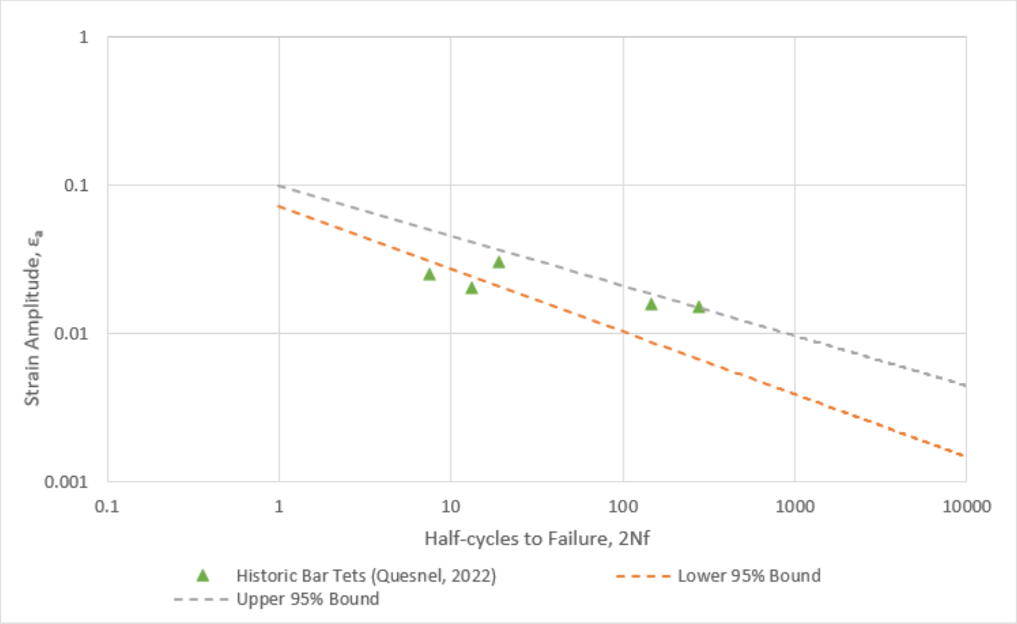

Figure 37: Historic bar tests (Quesnel, 2022) vs 95% bounds

To account for the wide range of variability in material properties and the relatively severe consequences of the limit state of reinforcement fracture, the probability of fracture plots were re-created using the probability of fracture two standard deviations above the mean reported in Figures 38-41. These probabilities represent a conservative upper bound on probability of fracture.

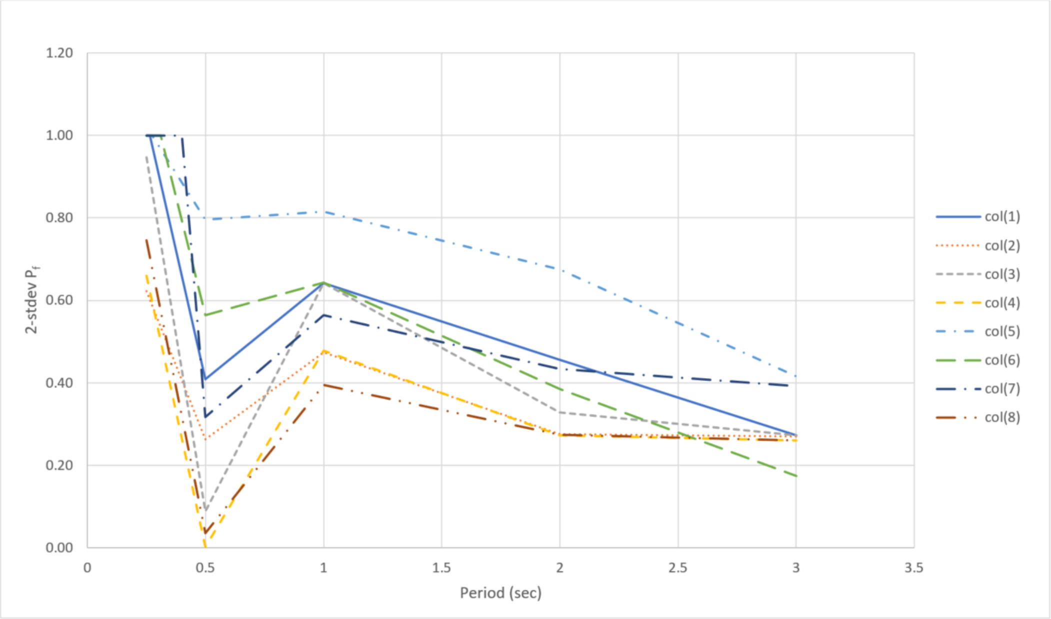

Figure 38: Location 2 – Ocean Shores, WA – Avg. + 2stdev P_f vs Period

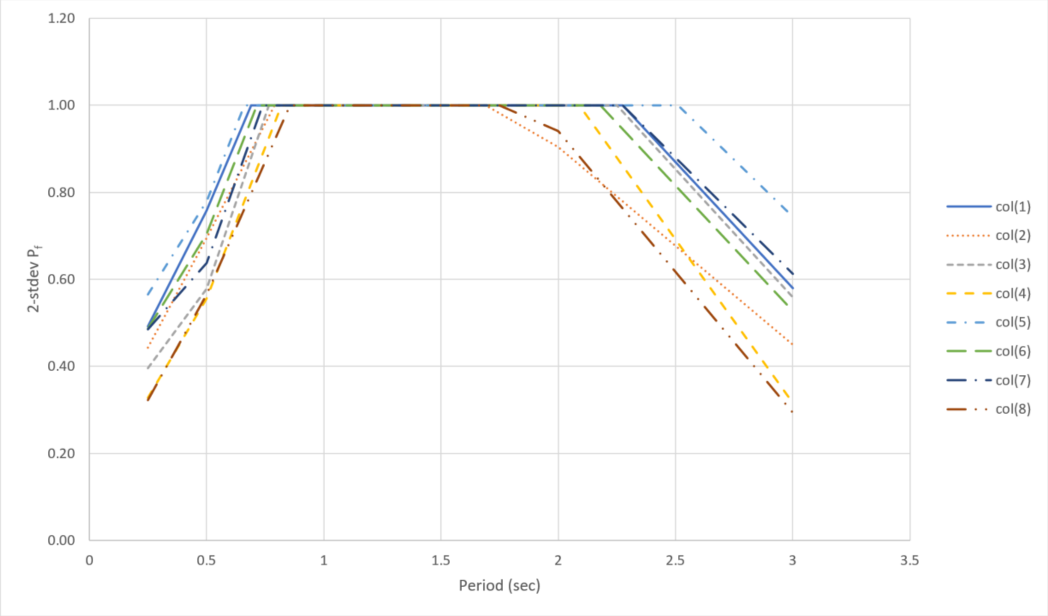

Figure 39: Location 3 – Port Angeles, WA – Avg. + 2stdev P_f vs Period

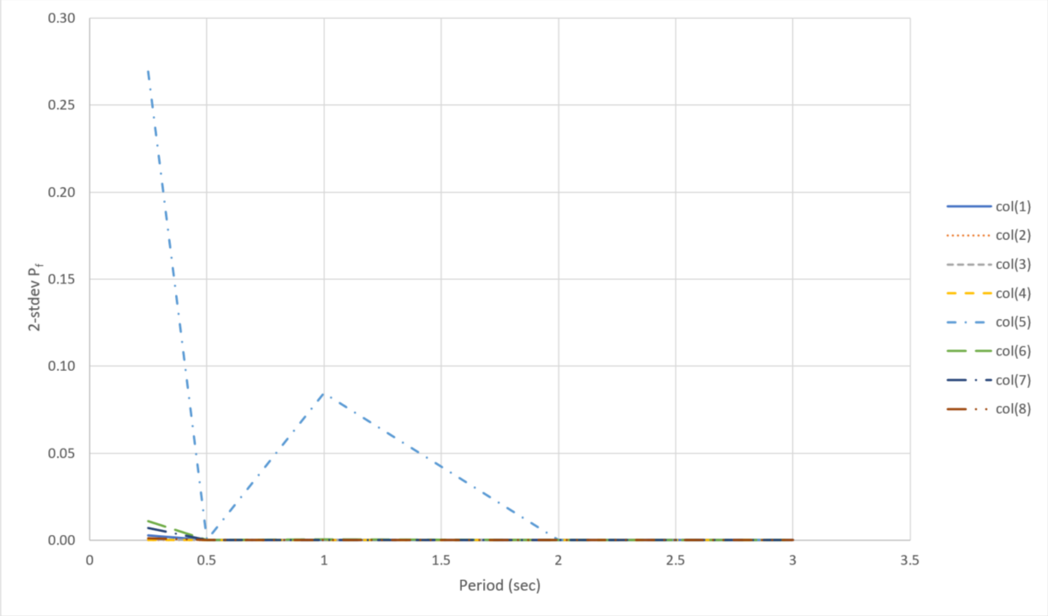

Figure 40: Location 4 – Olympia, WA – Avg. + 2stdev P_f vs Period

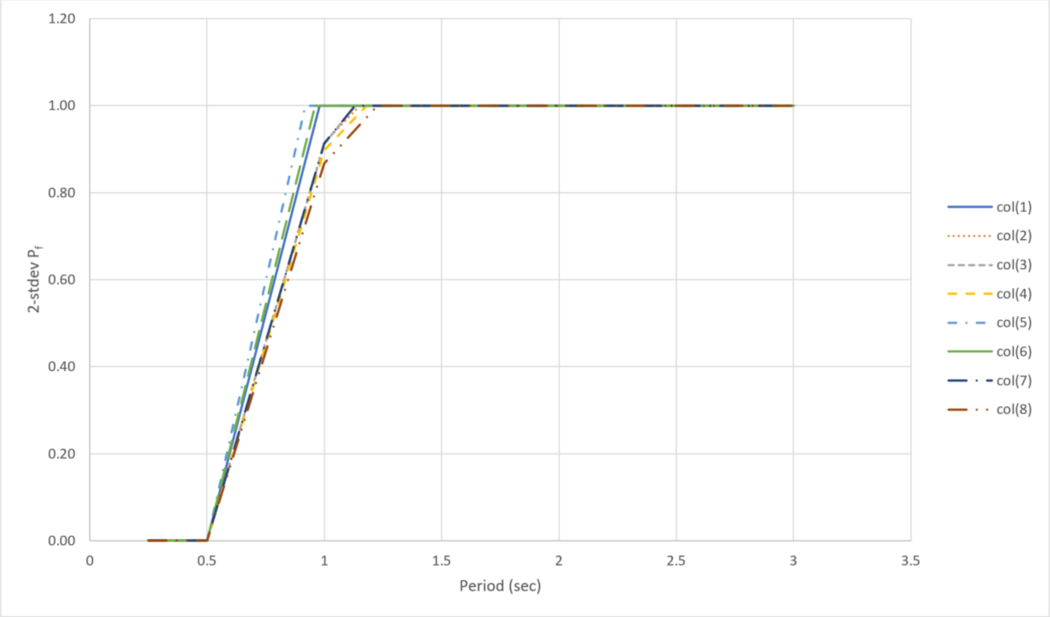

Figure 41: Location 8 – Seattle, WA – Avg. + 2stdev P_f vs Period

For the fragility of bar fracture two standard deviations above the mean, it is clear that for locations with a basin it is likely that a bar fracture will occur during a CSZ earthquake. However, for locations outside the basin, with low axial load ratio, it is still highly unlikely that a bar fracture will be seen. This should be put into context however with the Nickelson (2022) test data that showed that the columns did not lose significant axial load carrying capacity after a single bar fracture, but rather had to fracture almost all the longitudinal bars to force collapse. Therefore, while fracture may be likely for locations such as Seattle and Port Angeles, it does not necessarily mean that the probability of bridge collapse is also high. Rather, if a longitudinal bar fractures, that bridge will instead likely need to be replaced post-earthquake.

CONCLUSIONS

This research conducted experimental tests and probabilistic numerical analyses to understand low-cycle fatigue in longitudinal reinforcement used in retrofitted concrete bridge columns. Testing focused on failure prediction accuracy utilizing the Koh-Stephens model and Palmgren-Miner's damage rule on various types of loading scenarios. Constant and variable amplitude tests were conducted on #5 and #7 Grade 40 rebar provided by Nucor. From testing results, damage index was calculated using estimated Koh-Stephens parameters. Test results showed high test to test variability and strong dependence on the calibration parameters for model accuracy. The Koh-Stephens model was improved through this research by applying statistical methods to account for some of the material parameter uncertainty. Regressions for the average and 95% confidence intervals were created using historic bar test data, which facilitated Monte-Carlo simulation to get a range of predicted fracture probabilities for any given variable amplitude strain history.

The fracture prediction model incorporating material parameter uncertainty was then applied to column models of CFRP retrofitted bridge columns subjected to Cascadia Subduction Zone earthquakes for 4 locations across western WA. The column and fracture models provided quantitative estimation of the likelihood of longitudinal bar fracture during a CSZ earthquake. The probability of fracture was presented for the four locations across western WA for eight different bridge column details and from period ranges between 0.25 – 3.0 seconds. Both the mean probability of fracture and the probability of fracture 2 standard deviations above the mean were presented.

Probability of fracture results were highly dependent on the location, period, and bridge column details. Results of locations without a basin showed that coastal locations were more critical than inland locations due to closer proximity to the fault. However, locations with a basin had high probabilities of longitudinal bar fractures for bridge columns with periods between 1.0 - 3.0 seconds. These high probability of fracture results were greater than locations without a basin. Periods at which peak probability of fracture occurred increased as the basin effect became more severe; non-basin locations experienced peak probability of fracture at shorter periods less than 1.0 seconds, while deep basin locations experienced peak probability of fracture at longer periods between 1.0 and 3.0 seconds.

Column design and loading also affected the probability of fracture. Low reinforcement ratio combined with a high axial load ratio resulted in higher fracture probabilities compared to a heavily reinforced column with low axial load. This finding was consistent throughout all locations when all eight columns were compared. Increased ductility values resulted in higher probability of fracture also due to greater inelastic strain demand. However, analysis by Kortum (2021) determined that a majority of life-line route columns had ductility ratios between 2 and 3.5.

REFERENCES

Aldabagh, S., Shahria Alam, M. (2021). “Low-cycle fatigue performance of high strength steel reinforcing bars considering the effect of inelastic buckling.” *Engineering Structures* 235: 1-13.

Alsiwat, J. M., and Saatcioglu, M. (1992). Reinforcement Anchorage Slip under Monotonic Loading. Journal of Structural Engineering, 118(9), 2421–2438. https://doi.org/10.1061/(ASCE)0733-9445(1992)118:9(2421)

Arnold, L. (2023). Low-Cycle Fatigue Fracture Prediction of Grade 40 Reinforcing Steel Bars in Concrete Bridge Columns. M.S. Thesis, Washington State University, Pullman, WA.

ASTM E1049-85 (2011). “Standard Practices for Cycle Counting in Fatigue Analysis.” *Annual Book of ASTM Standards*, ASTM International, West Conshohocken, PA. Vol. 03.01, pp. 1-10.

Atwater, B. F., Nelson, A. R., Clague, J. J., Carver, G. A., Yamaguchi, D. K., Bobrowsky, P. T., Bourgeois, J., Darienzo, M. E., Grant, W. C., Hemphill-Haley, E., Kelsey, H. M., Jacoby, G. C., Nishenko, S. P., Palmer, S. P., Peterson, C. D., and Reinhart, M. A. (1995). “Summary of Coastal Geologic Evidence for Past Great Earthquakes at the Cascadia Subduction Zone.” Earthquake Spectra, 11(1), 1–18.

Barbosa, A. R., Trejo, D., Nielson, D., Mazerei, V. Tibbits, C. (2017). “High Strength Reinforcing Steel Bars: Low Cycle Fatigue Behavior.” Oregon State University, Salem OR. Report No. SPR 762.

Bell, S. (2022). “Modeled Behavior and Failure Probability of Steel Jacket Retrofitted Reinforced Concrete Bridge Columns in Cascadia Subduction Zone Earthquakes.” M.S. Thesis, Washington State University, Pullman, WA.

Brown, J. and Kunnath, S. K. (2004). “Low-Cycle Fatigue Failure of Reinforcing Steel Bars.” *ACI Materials Journal*, 101(6): 457-466.

Buckle, I.G. (1994). The Northridge, California Earthquake of January 17, 1994: Performance of Highway Bridges. Technical Report NCEER-94-0008, National Center for Earthquake Engineering Research, State University of New York at Buffalo, Buffalo, NY, 136 pp.

Chai, Y., Priestley, M., and Seible, F. (1991). Seismic Retrofit of Circular Bridge Columns for Enhanced Flexural Performance. *ACI Structural Journal*, *88*(5), 571–584. https://doi.org/10.14359/2759

Chai, Y., Priestley, M., and Seible, F. (1994). Analytical Model for Steel-Jacketed RC Circular Bridge Columns. *Journal of Structural Engineering*, *120*(8), 2358–2376. https://doi.org/10.1061/(ASCE)0733-9445(1994)120:8(2358)

Coffin Jr., L. F., (1954). “A Study of the Effects of Cyclic Thermal Stresses on a Ductile Metal.” *Journal of Fluids Engineering*, 76(6): 931-949.

De Zamacona Cervantes, G. E. (2019). “Response of Idealized Structural Systems to Simulated M9 Cascadia Subduction Zone Earthquakes Considering Local Soil Conditions.” M.S. Thesis, University of Washington, Seattle, WA.

Dowling, N. E. (2013). “Mechanical Behavior of Materials; Engineering Methods for Deformation, Fracture, and Fatigue.” 4th Edition. Pearson Education Inc., Upper Saddle River, NJ. pp. 450-456.

EERI (1990). Loma Prieta Earthquake Reconnaissance Report-(Supplement to Volume 6). Earthquake Spectra, Earthquake Engineering Research Institute, 448 pp.

EERI. (1994). Northridge Earthquake January 17, 1994, Preliminary Reconnaissance Report,” No. 94-01, J. F. Hall, ed., Earthquake Engineering Research Institute, Oakland, Calif., 1994, p. 104.

Elsanadedy, H. M., Al-Salloum, Y. A., Alsayed, S. H., and Iqbal, R. A. (2012). Experimental and numerical investigation of size effects in FRP-wrapped concrete columns. *Construction and Building Materials*, *29*, 56–72. https://doi.org/10.1016/j.conbuildmat.2011.10.025

Elwood, K. J., and Eberhard, M. O. (2009). Effective Stiffness of Reinforced Concrete Columns. *Structural Journal*, *106*(4), 476–484. https://doi.org/10.14359/56613

Federal Highway Administration (FHWA). (2006). Seismic Retrofitting Manual for Highway Structures: Part 1 – Bridges. U.S. Department of Transportation, Federal Highway Administration, Research, Development, and Technology, McLean, VA.

Frankel, A., Wirth, E., Marafi, N., Vidale, J., and Stephenson, W. (2018). “Broadband Synthetic Seismograms for Magnitude 9 Earthquakes on the Cascadia Megathrust Based On 3D Simulations and Stochastic Synthetics (Part 1): Methodology and Overall Results.” Bulletin of the Seismological Society of America, 108 (5A): 2347-2369.

Fung, G. G., Lebeau, R. J., Klein, E. D., Belvedere, J., and Goldschmidt, A. F. (1971). Field Investigation of Bridge Damage in the San Fernando Earthquake. Technical Report, Bridge Department, Division of Highways, California Department of Transportation, Sacramento, CA, 209 pp.

Goldfinger, C., Nelson, C. H., Morey, A. E., Johnson, J. E., Patton, J. R., Karabanov, E., Gutiérrez-Pastor, J., Eriksson, A. T., Gràcia, E., Dunhill, G., Enkin, R. J., Dallimore, A., and Vallier, T. (2012). Turbidite Event History—Methods and Implications for Holocene Paleoseismicity of the Cascadia Subduction Zone, U.S. Geological Survey Professional Paper 1661–F, 170 p.

Hawileh, R. A., Abdalla, J. A., Oudah, F., Abdelrahman K. (2009). “Low-cycle fatigue life behavior of BS 460B and BS B500B steel reinforcing bars”. *Fatigue & Fracture of Engineering Materials & Structures*, 33(7): 397-407.

Kashani, M. M., Barmi, A. K., Malinova, V. S. (2015). “Influence of inelastic buckling on low-cycle fatigue degradation of reinforcing bars.” *Construction of Building Materials*, 94: 644-655.

Koh, S. K. and Stephens, R. I. (1991). “Mean Stress Effects on Low Cycle Fatigue for a High Strength Steel.” *Fatigue Fract. Engng Mater. Struct*, 14(4): 413-428.

Kortum, Z. (2021). “Impacts of Cascadia Subduction Zone M9 Earthquakes on Bridges in Washington State: SDOF Idealized Bridges.” M.S. Thesis, University of Washington, Seattle WA.

Mander, J., Priestley, M., and Park, R. (1988). Theoretical Stress-Strain Model for Confined Concrete. *Journal of Structural Engineering, 114*(8), 1804–1826. https://doi.org/10.1061/(ASCE)0733-9445(1988)114:8(1804)

Mander, J. B., Panthaki, F. D., Kasalanati, A. (1994). “Low-Cycle Fatigue Behavior of Reinforcing Steel.” *Journal of Materials in Civil Engineering*, Vol. 6, No. 4, pp. 468.

Manson, S. S. (1953). “Behavior of Materials Under Conditions of Thermal Stress.” *Heat Transfer Symposium*, University of Michigan Engineering Research Institute, Ann Arbor, MI. pp 9-75.

McGuiness, S. (2021). Experimental Characterization of Steel Jacket Retrofitted Reinforced Concrete Bridge Column Behavior in Cascadia Subduction Zone Earthquakes. M.S. Thesis, Washington State University, Pullman, WA.

Mohammed, T. A. (2011). *Reinforced Concrete Structural Members Under Impact Loading* Thesis. University of Toledo. Toledo, NM. https://etd.ohiolink.edu/apexprod/rws_olink /r/1501/10?clear=10andp10_accession_num=toledo1321650443.

Nickelson, W. (2022). “Behavior of Carbon Fiber Reinforced Polymer Jacket Retrofitted Reinforced Concrete Bridge Columns in Cascadia Subduction Zone Earthquakes.” M.S. Thesis, Washington State University, Pullman, WA.

National Institute of Standards and Technology (NIST). (1990). Performance of Structures during the Loma Prieta Earthquake of October 17, 1989. NIST Publication 778, Jan. 1990.

Priestley, M.J.N., Seible, F., Xiao, Y., and Verma, R. (1994a). Steel Jacket Retrofitting of Reinforced Concrete Bridge Columns for Enhanced Shear Strength—Part 1: Theoretical Considerations and Test Design. ACI Structural Journal, 91(4): 394-405.

Priestley, M.J.N., Seible, F., Xiao, Y., and Verma, R. (1994b). Steel Jacket Retrofitting of Reinforced Concrete Bridge Columns for Enhanced Shear Strength—Part 2: Test Results and Comparison with Theory. ACI Structural Journal, 91(5): 537-551.

Quesnel, Z. J. (2022). “Low-cycle Fatigue Behavior of Modern and Historic Grade 40 Reinforcing Steel Bars.” M.S. Thesis, Washington State University, Pullman, WA.

Youssf, O., ElGawady, M. A., and Mills, J. E. (2015). Displacement and plastic hinge length of FRP-confined circular reinforced concrete columns. *Engineering Structures, 101,* 465–476. https://doi.org/10.1016/j.engstruct.2015.07.026

Youssf, O., ElGawady, M. A., Mills, J. E., and Ma, X. (2014). Finite element modelling and dilation of FRP-confined concrete columns. *Engineering Structures*, *79,* 70–85. https://doi.org/10.1016/j.engstruct.2014.07.045

Zhao, J., and Sritharan, S. (2007). Modeling of Strain Penetration Effects in Fiber-Based Analysis of Reinforced Concrete Structures. *Structural Journal*, *104*(2), 133–141. https://doi.org/10.14359/18525

Xie, Y. (2013). "Lecture 12 Linear Regression: Test and Confidence Intervals." H. Milton Stewart School of Industrial Systems & Engineering, Georgia Institute of Technology, Atlanta GA.

APPENDIX ONE

Table A1.1. Literature test data used to create fracture prediction model

Mander et al (1994)		
ε_a	$2n_f$	**Bar Size**
0.17	0.5	5
0.04	5	5
0.03	8.2	5
0.025	11.2	5
0.02	18.4	5
0.0175	26	5
0.015	42	5
0.0134	50	5
0.0125	46	5
0.01	98	5
0.008	296	5

Quesnel (2021)		
ε_a	$2n_f$	**Bar Size**
0.0225	105.4	5
0.04	42	5
0.06	9.4	5
0.05	17	7
0.03	92	7
0.02	108	7
0.03	105	7
0.04	38	7

Brown et al (2004)		
ε_a	$2n_f$	**Bar Size**
0.015	87.0	6
0.015	91.0	6
0.0175	61.0	6
0.02	53.0	6
0.02	49.0	6
0.0225	44.0	6
0.025	29.0	6
0.025	30.0	6
0.03	22.0	6
0.015	54.0	6
0.015	61.0	6
0.0175	40.0	6
0.02	34.0	6
0.02	27.0	6
0.0225	28.0	6
0.025	21.0	6
0.025	19.0	6
0.03	11.0	6
0.03	14.0	6
0.015	92.0	7
0.015	99.0	7
0.0175	61.0	7
0.0175	95.0	7
0.02	46.0	7
0.02	54.0	7
0.0225	42.0	7
0.0225	44.0	7
0.025	38.0	7
0.025	38.0	7
0.0275	22.0	7
0.03	24.0	7
0.03	21.0	7
0.015	111	8
0.015	117.0	8
0.0175	78.0	8
0.0175	70.0	8
0.02	61.0	8
0.02	52.0	8
0.0225	44.0	8
0.0225	41.0	8
0.025	28.0	8
0.025	32.0	8
0.0275	25.0	8
0.03	16.0	8
0.03	15	8
0.015	127.0	9
0.015	134.0	9
0.0175	90.0	9
0.0175	83.0	9
0.02	63.0	9
0.02	55.0	9
0.0225	38.0	9
0.025	23.0	9
0.025	25.0	9
0.0275	19.0	9
0.03	15.0	9
0.03	18.0	9

APPENDIX TWO

Table A2.1. Bin ranges of strain amplitude in fracture prediction model

Bin ID	Start Value	End Value
1	0	0.00125
2	0.00125	0.0025
3	0.0025	0.00375
4	0.00375	0.005
5	0.005	0.00625
6	0.00625	0.0075
7	0.0075	0.00875
8	0.00875	0.01
9	0.01	0.01125
10	0.01125	0.0125
11	0.0125	0.01375
12	0.01375	0.015
13	0.015	0.01625
14	0.01625	0.0175
15	0.0175	0.01875
16	0.01875	0.02
17	0.02	0.02125
18	0.02125	0.0225
19	0.0225	0.02375
20	0.02375	0.025
21	0.025	0.02625
22	0.02625	0.0275
23	0.0275	0.02875
24	0.02875	0.03
25	0.03	0.03125
26	0.03125	0.0325
27	0.0325	0.03375
28	0.03375	0.035
29	0.035	0.03625
30	0.03625	0.0375
31	0.0375	0.03875
32	0.03875	0.04
33	0.04	0.0425
34	0.0425	0.045
35	0.045	0.0475
36	0.0475	0.05
37	0.05	0.0525
38	0.0525	0.055
39	0.055	0.0575
40	0.0575	0.06
41	0.06	0.0625
42	0.0625	0.065
43	0.065	0.0675
44	0.0675	0.07
45	0.07	0.0725
46	0.0725	0.075
47	0.075	0.0775
48	0.0775	0.08
49	0.08	0.0825
50	0.0825	0.085
51	0.085	0.0875
52	0.0875	0.09
53	0.09	0.0925
54	0.0925	0.095
55	0.095	0.0975
56	0.0975	0.1
57	0.1	>0.1